Mechanical bistability enabled by ectodermal compression facilitates *Drosophila* mesoderm invagination

Hanqing Guo[1], Michael Swan[2], Shicheng Huang[1] and Bing He[1]*

1. Department of Biological Sciences, Dartmouth College, Hanover, NH
2. Department of Molecular Biology, Princeton University, Princeton, NJ

*Correspondence: Bing.He@dartmouth.edu

Abstract

Apical constriction driven by non-muscle myosin II ("myosin") provides a well-conserved mechanism to mediate epithelial folding. It remains unclear how contractile forces near the apical surface of a cell sheet drive out-of-plane bending of the sheet and whether myosin contractility is required throughout folding. By optogenetic-mediated acute inhibition of myosin, we find that during *Drosophila* mesoderm invagination, myosin contractility is critical to prevent tissue relaxation during the early, "priming" stage of folding but is dispensable for the actual folding step after the tissue passes through a stereotyped transitional configuration, suggesting that the mesoderm is mechanically bistable during gastrulation. Combining computer modeling and experimental measurements, we show that the observed mechanical bistability arises from an in-plane compression from the surrounding ectoderm, which promotes mesoderm invagination by facilitating a buckling transition. Our results indicate that *Drosophila* mesoderm invagination requires a joint action of local apical constriction and global in-plane compression to trigger epithelial buckling.

Introduction

Contractile forces generated by actin and myosin ("actomyosin") networks are widely employed in embryogenesis to drive cell motility and cell shape change that pattern epithelial tissues[1,2]. During epithelial folding driven by apical constriction, the actomyosin network in epithelial cells constricts cell apices, which leads to bending of the cell sheet[3]. It remains unclear how "in-plane" contractile forces generated at the apical surface drives "out-of-the-plane" bending of the tissue. The invagination of the presumptive mesoderm during *Drosophila* gastrulation is a well-characterized epithelial folding processes mediated by apical constriction[4–6]. During gastrulation, ventrally localized mesoderm precursor cells constrict their cell apices and become internalized into a ventral furrow, which occurs in two steps[7,8]. During the first 10 – 12 minutes, the ventral cells undergo apical constriction and elongate in the apical-basal direction, while the cell apices remain near the surface of the embryo ("the lengthening phase"). In the next 6 – 8 minutes, the ventral cells rapidly internalize as they shorten back to a wedge-like morphology ("the shortening phase") (Figure 1a). Ventral furrow formation is controlled by the dorsal-ventral patterning system, which induces the recruitment of RhoGEF2, a guanine nucleotide exchange factor (GEF) for Rho1 (*Drosophila* homologue of the small GTPase RhoA), to the apical pole of mesoderm precursor cells via G-protein coupled receptor (GPCR) signaling[9–14]. RhoGEF2 in turn activates myosin at the apical surface through the RhoGEF2-Rho1-Rho associated kinase (Rok) pathway[15–20]. Activated myosin forms a supracellular actomyosin network across the apical surface of the prospective mesoderm and drives the constriction of cell apices[1,19,21].

The essential role of apical constriction in ventral furrow formation has been well demonstrated[1]. Genetic mutations or pharmacological treatments that inhibit myosin activity disrupt apical

constriction and result in failure in ventral furrow formation[5,6]. Biophysical studies show that cell shape change occurring during the lengthening phase is a direct, viscous response of the tissue interior to apical constriction[22,23]. However, it remains unclear whether apical constriction also directly drives invagination during the shortening phase. The observation that the maximal rate of apical constriction and the maximal rate of tissue invagination occur at distinct times suggests that apical constriction does not directly cause tissue invagination[24,25]. A number of computational models also predict that mesoderm invagination requires additional mechanical input, such as "pushing" forces from the surrounding ectodermal tissues, but experimental evidence for this additional mechanical input remains sparse[26–29].

To determine whether actomyosin contractility is required throughout the folding process and to identify potential actomyosin independent contributions for invagination, we developed an optogenetic tool to acutely inhibit myosin activation. We find that the mesoderm primordium is mechanically bistable during gastrulation: acute loss of myosin contractility during most of the lengthening phase results in immediate relaxation of the constricted tissue, but similar treatment near or after the lengthening-shortening transition does not impede invagination. This bipartite response to myosin inhibition is reminiscent of the outcome of eliminating the transverse "indentation force" during buckling of a compressed elastic beam. Combining computer modeling with biophysical measurements and tissue manipulations, we present both theoretical and experimental evidence that mesoderm invagination is enabled by an in-plane compression from the surrounding ectodermal tissue, which function in parallel with apical constriction to trigger buckling of the mesoderm.

Results

Plasma membrane recruitment of Rho1DN results in rapid loss of cortical myosin

In order to acutely inhibit myosin activity in live embryos (Figure 1a), we generated an optogenetic tool, "Opto-Rho1DN", to inhibit Rho1 through light-dependent plasma membrane recruitment of a dominant negative form of Rho1 (Rho1DN). Like other Rho GTPases, Rho1 cycles between an active, GTP-bound state and an inactive, GDP-bound state[30]. Rho1DN bears a T19N mutation, which abolishes the ability of the mutant protein to exchange GDP for GTP and thereby locks the protein in the inactive state[15]. A second mutation in Rho1DN, C189Y, abolishes its naive membrane targeting signal[31,32]. When Rho1DN is recruited to the plasma membrane, it binds to and sequesters Rho1 GEFs, thereby preventing activation of endogenous Rho1 as well as Rho1-Rok-mediated activation of myosin[15,33].

Opto-Rho1DN is based on the CRY2-CIB light-sensitive dimerization system[34–36] (Figure 1b). The tool contains two components: a GFP-tagged N-terminal of CIB1 protein (CIBN) anchored at the cytoplasmic leaflet of the plasma membrane (CIBN-pmGFP)[36], and a fusion protein between Rho1DN, an mCherry tag, and a light-reactive protein CRY2 (CRY2-Rho1DN). CRY2-Rho1DN remained in the cytoplasm when the sample was kept in dark or imaged with a yellow-green (561-nm) laser (Figure 1c, T = 0). Upon blue (488-nm) laser stimulation, CRY2 undergoes a conformational change and binds to CIBN[34,35], resulting in rapid recruitment of CRY2-Rho1DN to the plasma membrane (Figure 1c, d; Movie 1). The average time for half-maximal membrane recruitment of CRY2-Rho1DN was 4 seconds (3.9 ± 2.8 sec, mean ± s.d., n = 5 embryos). Embryos expressing CIBN-pmGFP and CRY2-Rho1DN developed normally in a dark environment and could hatch (100%, n = 63 embryos). In contrast, most embryos (>85%, n = 70

embryos) kept in ambient room light failed to hatch, reflecting the essential role of Rho1 in *Drosophila* embryogenesis[15,37,38].

The effectiveness of Opto-Rho1DN on myosin inactivation was validated by stimulation of embryos during apical constriction, which resulted in diminishing of apical myosin signal within 60 seconds (Figure 1e, f; Movie 2). Rapid disappearance of cortical myosin upon Rho1 inhibition is consistent with the notion that Rho1 and myosin cycle quickly through active and inactive statues due to the activity of GTPase activating proteins (GAPs) for Rho1 and myosin light chain phosphatases, respectively[39,40]. Our data also provide direct evidence that sustained myosin activity during ventral furrow formation requires persistent activation of Rho1. Consistent with the myosin phenotype, we found that Opto-Rho1DN stimulation before or during apical constriction results in prevention or reversal of apical constriction, respectively (Supplementary Figure 1). By stimulating the embryo within a specific region of interest, we show that membrane recruitment of CRY2-Rho1DN and inhibition of apical constriction were restricted to cells within the stimulated region (Figure 1g, Supplementary Figure 1c, d).

In addition to myosin activation, Rho1 signaling also regulates several other cellular processes that may impact apical constriction, including actin assembly through the formin protein Diaphanous and adherens junction remodeling through various mechanisms[38,41–43]. However, the rapid cortical myosin loss and tissue relaxation upon Opto-Rho1DN stimulation is most likely caused by myosin inactivation, as a similar phenotype was observed in embryos injected with the Rok inhibitor but not in embryos mutant for Diaphanous or adherens junction

components[20,21,40,44]. Taken together, our results indicate that Opto-Rho1DN is an effective tool for spatial and temporally confined inactivation of actomyosin contractility.

Acute inhibition of myosin contractility reveals mechanical bistability of the mesoderm during gastrulation

Using Opto-Rho1DN, we determined the role of actomyosin contractility at different stages of ventral furrow formation. We first obtained non-stimulated control movies by imaging embryos bearing Opto-Rho1DN on a multiphoton microscope using a 1040-nm pulsed laser, which excites mCherry but does not stimulate CRY2[36]. Without stimulation, the embryos underwent normal ventral furrow formation (Figure 2a). The transition from the lengthening phase to the shortening phase ($T_{L\text{-}S\ trans}$) occurred around ten minutes after the onset of gastrulation (9.3 ± 1.6 minutes, mean ± s.d., n = 10 embryos), which was similar to the wildtype embryos (9.2 ± 1.3 minutes, mean ± s.d., n = 7 embryos) (Supplementary Figure 2a-c). This transition was characterized by a rapid inward movement of the apically constricted cells and could be readily appreciated by the time evolution of distance between the cell apices and the vitelline membrane of the eggshell (invagination depth “D”, Supplementary Figure 2d).

Next, we examined the effect of Opto-Rho1DN stimulation on furrow invagination (Methods). To minimize the impact of embryo-to-embryo variation in $T_{L\text{-}S\ trans}$ (Supplementary Figure 2d), we temporally aligned each post-stimulation movie to a representative control movie based on the intermediate furrow morphology at the time of stimulation (Figure 2b; Supplementary Figure 2e; Methods). Measuring the rate of furrow invagination (dD/dt) immediately after stimulation revealed three types of tissue responses to stimulation (Figure 2a, b; Supplementary Figure 2f, g;

Movie 3). For most embryos that were stimulated before T = 7 minutes ("Early Group" embryos), the constricting cells relaxed immediately. The initial apical indentation disappeared ($dD/dt < 0$). The expanded apical domain of the flanking, non-constricting cells shrunk back, indicating that the apical cell cortex was elastic (Supplementary Figure 3a, b). In contrast, for most embryos that were stimulated after T = 7 minutes ("Late Group" embryos), furrow invagination proceeded at a normal rate and dD/dt remained positive. Finally, some embryos stimulated around T = 7 minutes (6.5 ± 1.4 minutes, mean ± s.d., n = 4 embryos; "Mid Group" embryos) displayed an intermediate phenotype, where ventral furrow invagination paused for around five minutes (4.7 ± 0.5 minutes; $dD/dt \approx 0$) before invagination resumed. We confirmed that there was not residual apical myosin in Late Group embryos upon stimulation (Supplementary Figure 4a). Furthermore, myosin accumulated at lateral membranes of constricting cells, which has been shown to facilitate furrow invagination[29,45,46], also quickly disappeared after stimulation (Supplementary Figure 4b, c). Therefore, furrow invagination in Late Group embryos is not due to myosin activities at the apical or lateral cortices of the mesodermal cells. Together, these results indicate that actomyosin contractility is required in the early but not the late phase of furrow formation. The narrow time window when Mid Group embryos were stimulated defined the "transition phase" for sensitivity to myosin inhibition (T_{trans}), which is immediately before $T_{L\text{-}S\ trans}$ (Figure 2c).

While all Early Group embryos showed tissue relaxation after stimulation, 5 out of 8 of them were able to invaginate after a prolonged delay (Figure 2b; Supplementary Figure 3c-f). The invagination was associated with limited myosin reaccumulation at the cell apices occurring approximately ten minutes after the initial stimulation (Supplementary Figure 3e-f). It is unclear

why apical myosin sometimes reoccurred in the presence of persistent membrane localization of CRY2-Rho1DN. Nevertheless, the completion of furrow invagination when apical constriction is partially impaired is consistent with previous genetic studies and suggests that invagination is facilitated by additional mechanical input[10,11].

Because the response of ventral furrow formation to myosin inhibition appears to be bipartite, we sought to identify morphological features of the progressing furrow that associate with T_{trans}. Hence, we examined the relationship between D immediately after stimulation ("D_s") and the extent by which furrow invagination is affected (assessed by the delay time in furrow invagination, T_{delay}, see Methods). We found that for stimulated embryos, T_{delay} was ultrasensitive to D_s, with a steep transition at around 6 μm (Figure 2d). When D_s was above the threshold, T_{delay} was close to 0. When D_s was below the threshold, T_{delay} increased to ten minutes (9.4 ± 1.4 minutes, mean ± s.d., n = 5 Early Group embryos) or longer (fail to invaginate, n = 3 Early Group embryos). Therefore, the response to acute myosin inhibition can be well predicted by the tissue morphology associated with the stage of furrow progression.

The bipartite response of the embryo to acute myosin inhibition suggests that the mesoderm during gastrulation is mechanically bistable and has two stable equilibrium states: the initial, pre-constricted conformation and the final, fully invaginated conformation (Figure 2e). Energy input from actomyosin-mediated apical constriction drives the transition from the initial state to an intermediate state (T_{trans}), which has the propensity to transition into the final state without further requirement of actomyosin contractility. If myosin is inhibited before T_{trans}, the furrow

will relax back to the initial state. In contrast, if myosin is inhibited after T_{trans}, the furrow will continue to invaginate without pause (Figure 2e).

Mechanical bistability of the mesoderm during gastrulation can arise from ectoderm-derived compressive stresses

In the search for additional mechanism(s) that may facilitate furrow invagination, we considered a potential role for elastic cell shortening forces as suggested by a previous computer model[24]. The Polyakov et al. model proposed that cell shortening and tissue invagination can be driven by release of elastic energy stored in the lateral cortices when cells undergo apical constriction and cell lengthening (Figure 3a). Using this model, we simulated the effect of acute myosin loss by removing the apical contractile forces at different intermediate states of the model (Methods). We found that regardless of the stage when apical constriction was eliminated, the model always returned to its initial configuration (Figure 3c). This result does not support the hypothesis that the bistable characteristic of the mesoderm arises from lateral restoring forces in the cells undergoing apical constriction.

What alternative mechanism may account for mechanical bistability in the folding process? The bistable characteristic of the mesoderm is reminiscent of a compressed elastic beam undergoing snap-through buckling facilitated by a transverse "indentation force" (Figure 3b) [47]. Based on this analogy, we hypothesized that mesoderm invagination is mediated through tissue buckling enabled by in-plane compressive stresses. We tested this hypothesis by implementing compressive stresses from the ectoderm (Figure 3a; Methods). In the presence of ectodermal compression, the model recapitulated the bipartite response to loss of apical constriction as

observed experimentally (Figure 3c). In particular, the transitional state of the tissue revealed in the simulation is nearly identical to that identified in our optogenetic experiments. Therefore, buckling of an elastic cell sheet can well reproduce the bistable characteristics of the mesoderm observed in real embryos. Our model also predicts that the presence of ectodermal compression could compensate for partial impairment of apical constriction (Figure 3d), which explains why some Early Group embryos could still invaginate when myosin activity was greatly downregulated.

Interestingly, our simulation predicts that for embryos stimulated after T_{trans}, the ventral furrow at the final invaginated state would be narrower with fewer cells being incorporated into the furrow compared to control embryos, similar to what we observed in Late Group embryos (Figure 3c; Supplementary Figure 5a, b). In these embryos, stimulation induced a mild but noticeable alteration in tissue flow that indicates the occurrence of apical relaxation in the constricted cells (Supplementary Figure 5c, d). These results suggest that maintaining actomyosin contractility after T_{trans} helps to prevent local relaxation of the apical membranes, thereby allowing more cells to be incorporated into the furrow. This “late” function of actomyosin contractility is dispensable for furrow invagination per se but is important for the complete internalization of the prospective mesoderm.

The lateral ectoderm becomes compressive prior to T_{trans}

Our hypothesis predicts that during gastrulation the ectodermal tissue outside of the mesodermal region is compressive. To test this prediction, we used laser microdissection to soften a group of ectodermal cells on the lateral side of the embryo without disrupting their cell membranes

(Figure 4a; Methods). If the tissue is compressive, we would expect to see an immediate shrinkage of the treated region (Figure 4b). To quantify the tissue response, we measured the rate of width change in the laser treated regions (Figure 4c, d; Methods). Microdissection within the first 5 minutes of gastrulation resulted in no obvious tissue shrinkage. In contrast, the treated region immediately shrunk when microdissection was performed 5 to 10 minutes into gastrulation, while the control non-treated region was unaffected (Figure 4e-g; Movie 4). Our results indicate that in-plane compressive stresses are built up in the lateral ectoderm shortly before T_{trans}, which supports the hypothesis that mesoderm invagination is facilitated by ectodermal compression (Figure 4h).

In theory, the presence of compressive stresses in the ectoderm should result in displacement of the ectodermal cells towards the ventral side independent of mesoderm invagination. The Early Group embryos provided an opportunity for us to examine whether apical constriction-independent movement of the lateral ectoderm exists. Our measurements confirmed the "reverse" movement of the ventral cells during tissue relaxation (Supplementary Figure 6). Meanwhile, the lateral ectoderm moved in the opposite direction towards the ventral midline (Supplementary Figure 6). This finding is consistent with a previous study showing that ventral movement of the lateral ectoderm still occurred in mesoderm specification mutants that do not form ventral furrow[25]. Our results further demonstrate that this decoupling of movement can be observed without altering initial cell fate specification. These observations provide additional evidence to support the existence of ectodermal compression prior to T_{trans}.

What is the source of the compressive stresses in the lateral ectoderm? No cell division happens during ventral furrow formation[48,49], thereby excluding a role for cell proliferation in generating compressive stresses as seen in many other tissues[50]. Interestingly, it has been reported that ectodermal cells undergo apical-basal shortening during gastrulation[29], which could generate compressive stresses in the planar direction. However, it is also possible that ectodermal shortening is merely a passive response to mesoderm invagination as the surface area of the ectoderm increases. We measured the thickness of the lateral ectoderm and found our measurements does not support the latter scenario, because the onset of ectodermal shortening was generally earlier than $T_{L\text{-}S\ trans}$ (Supplementary Figure 7). Future development of approaches that can specifically inhibit ectodermal shortening would be essential for testing whether it plays an important role in mesoderm invagination.

Vertex dynamics model incorporating both apical constriction and ectodermal compression recapitulates tissue dynamics during ventral furrow formation

In addition to the bistable characteristic, another outstanding signature of buckling is the acceleration of deformation when the system passes through a threshold configuration[51]. Consistent with previous reports[24,25,45], our measurement of the speed of tissue movement indeed revealed a rapid acceleration of tissue deformation near T_{trans}, which was reflected by a steep increase in the rates of furrow invagination and ventral movement of the lateral ectoderm (Figure 5a-c; Movie 5). To test whether the buckling-like tissue dynamics can arise from a combined action of apical constriction and in-plane compression, we performed a modeling analysis simulating the characteristics of a ring-shaped elastic monolayer confined in a circular shell. In this 2D vertex dynamics model, the elastic monolayer was composed of square-shaped cells that

resist deformation (Figure 5d; Supplementary Figure 8; Methods). For convenience, we refer to the region of the monolayer where apical constriction occurs as the mesoderm and the region outside of the constriction domain as the ectoderm. The ectodermal cells could generate in-plane compressive stresses by moderately constricting their lateral edges (Methods). This model allowed us to study the dynamics of deformation over time, which was not possible with the Polyakov et al. model where energy minimization was used to drive model evolution (Figure 3) [24]. While the difference in cell geometry between the model and the real embryo precludes a quantitative comparison of the predicted and observed furrow morphology, this minimalistic approach allowed us to test the central concept of our hypothesis.

The model was driven out of the initial equilibrium configuration when the ventral mesodermal cells underwent apical constriction. Before ectodermal compression emerged, apical constriction reduced the apical area of the constricting cells by approximately 50% and resulted in a small apical indentation at the site of constriction (Figure 5e, T = 0 to T = 750; Supplementary Figure 8g, h; Movie 6). As ectodermal compression commenced, this intermediate configuration rapidly transitioned into a deeply invaginated configuration (Figure 5e, T = 750 to T = 1350; Movie 6). This transition was characterized by a steep increase in the invagination depth D and a rapid acceleration of the ventral movement of the lateral ectodermal cells, both of which closely resembled the real tissue dynamics (comparing Figure 5c and 5f). In the model, the extent of tissue acceleration was determined by the magnitude of ectodermal compression (Supplementary Figure 9a). In particular, the lack of compression caused the model to arrest at the intermediate, shallow-indentation stage (Figure 5g, h). Although the requirement for ectodermal compression in invagination could be partially bypassed by reducing the elastic strength of the monolayer, in

such circumstances, mesoderm invagination was less potent and became decoupled from ectodermal movements, thereby no longer representing the real tissue dynamics (Supplementary Figure 9b). Together, these results demonstrate that the characteristic tissue dynamics during ventral furrow formation can be recapitulated by a buckling process jointly mediated by apical constriction and in-plane compression.

Laser ablation of the lateral ectoderm results in a pause of mesoderm invagination at T_{trans}

Our model predicts that disruption of ectodermal compression will cause the furrow to arrest at the transition stage. To test this prediction, we examined the role of ectodermal tissue in mesoderm invagination by mechanically isolating the mesoderm within the embryo. To achieve this, we took advantage of the special form of cleavage ("cellularization") in early *Drosophila* embryos. During cellularization, plasma membrane furrows invaginate from the embryo surface and partition the peripherally localized syncytial nuclei into individual cells (Figure 6a) [52]. We used laser ablation to disrupt cell formation in the lateral ectodermal regions during early cellularization (Figure 6a; Methods). When cellularization completed in the untreated region, the prospective mesoderm was physically separated from the remaining, more dorsally localized ectodermal tissue. We found that the isolated mesoderm still underwent apical constriction, albeit with a moderately reduced rate (Figure 6c-e). However, the isolated mesoderm either arrested at the transition stage for a prolonged time or failed to invaginate (Figure 6b, c). This is in contrast to control embryos where the constricting cells were promptly internalized when their apical area reduced to approximately 40% of the original size (Figure 6c, d). To quantify the delay at the transition phase, we measured the interval between the time when the ventral cells reached 45% constriction and the time when the embryo reached an invagination depth D of 7 μm ("Delta T",

Figure 6f). Delta T increased from 4.7 ± 1.5 min in the control embryos to 22.9 ± 9.5 min in the ablated embryos that eventually invaginated (mean ± s.d., control: N = 3 embryos, ablated: N = 5 embryos, Figure 6g). Note that 2 out of 7 ablated embryos never reached a D of 7 μm. Importantly, the arrest at T_{trans} was not due to a reduced rate of apical constriction, because depleting myosin heavy chain Zipper (Zip) in early embryos did not cause any delay at the transition stage despite the markedly reduced rate of apical constriction (Supplementary Figure 10) [23]. These results are consistent with our model predicting that disruption of ectodermal compression during mesoderm invagination results in an arrest at T_{trans}.

Taken together, our combined modeling and experimental analyses find that ectodermal compression facilitates mesoderm invagination by exploiting mechanical bistability analogous to an elastic buckling process (Figure 7). *Drosophila* ventral furrow formation is a robust process in that it can still happen in various scenarios when apical constriction is weakened[7,10,12,53]. Recent studies have revealed that the supracellular actomyosin network is intrinsically robust, with build-in redundancies to secure global connectivity of the network[53]. Mechanical bistability of the mesoderm enabled by ectodermal compression provides an alternative, tissue-extrinsic mechanism that allows proper invagination of the mesoderm when apical actomyosin network is impaired due to genetic and environmental variations (e.g., Early Group and *zip RNAi* embryos).

Discussion

The canonical model for apical constriction-mediated cell sheet folding emphasizes the role of active cell deformation and suggests that the transformation of the cells from columnar shape to wedge shape through apical constriction "is sufficient to pull the outer surface of the cell sheet inward and to maintain invagination"[54]. Our study on *Drosophila* ventral furrow formation, however, suggests a different scenario. Using the Opto-Rho1DN optogenetic tool described in this work, we show that while actomyosin-mediated active cell deformation is critical for mesoderm invagination, after the initial apical constriction mediated "priming" stage, the subsequent rapid invagination step can take place in the absence of actomyosin contractility. Combining computer modeling and experimental data, we further show that ventral furrow formation is facilitated by mechanical bistability of the mesoderm during gastrulation, which arises from an in-plane compression from the surrounding ectodermal tissue. Our proposed tissue buckling mechanism addresses how "in-plane" apical contractile forces can drive the out-of-plane tissue bending and explains why mesoderm folding could still occur in mutants where apical constriction is partially impaired.

In principle, bending of a cell sheet can be achieved through two general mechanisms. In the first mechanism, an active cell deformation (e.g. apical constriction) that results in cell wedging can cause the tissue to acquire a folded configuration. In this case, the mechanism is tissue autonomous and does not necessarily require active mechanical contributions from neighboring tissues. In the second mechanism, bending of a cell sheet is prompted by an increase in the compressive stresses within the tissue[55]. This mechanism is tissue non-autonomous and depends on the tissues surrounding the region where folding happens. Our work suggests that ventral

furrow formation involves both tissue autonomous and non-autonomous mechanisms. Apical constriction within the mesodermal tissue brings the tissue to an intermediate, transitional state, thereby "priming" the tissue for folding, whereas in-plane compression from the surrounding ectodermal tissue facilitates the subsequent transition to the final, fully invaginated state through buckling. Our proposed mechanism is supported by the following findings. First, we present, as far as we know, the first experimental evidence that the lateral ectoderm becomes compressive shortly before the transition phase. Second, using computer modeling, we show that a combined action of apical constriction in the mesoderm and in-plane compression from the ectoderm can precisely reproduce the bipartite tissue response to acute loss of myosin contractility as well as the buckling-like tissue dynamics during ventral furrow formation. Finally, we show that the presence of the ectodermal tissues surrounding the mesoderm is critical for triggering the buckling transition from apical constriction to invagination. Together, these observations reveal an intimate coupling between the tissue autonomous and nonautonomous mechanisms during ventral furrow formation. The generation of ectodermal compression increases the buckling propensity of the epithelium, whereas the active cell shape change induced by apical constriction triggers buckling at a defined position. The requirement for this tissue level cooperation may explain the recent data showing that ectopic activation of Rho1 activity at different regions of cellular blastoderms in *Drosophila* results in different final furrow morphology[56].

The source of ectodermal compression during ventral furrow formation remains to be determined. In addition to the apical-basal shortening of the lateral ectoderm, previous studies showed that the dorsal cells undergo apical expansion during ventral furrow formation, suggesting a potential cell fate specific mechanism for ectodermal compression[25]. In addition,

other morphogenetic processes happening during gastrulation, such as posterior midgut invagination and cephalic furrow formation, might also contribute to the generation of tissue compression[25]. These studies indicate that the observed elevation of in-plane compressive stresses may be attributed to multiple processes happening simultaneously in gastrulating embryos.

The use of tissue compression may represent a common strategy to facilitate tissue internalization during gastrulation in *Drosophila* and related insects. In the midge *Chironomus riparius*, the internalization of the mesoderm occurs through uncoordinated cell ingression instead of invagination, which is due to the lack of two upstream regulators of actomyosin contractility, Fog and T48[57]. It is attractive to propose that ectodermal compression-enabled mechanical bistability also provide a mechanism to facilitate mesoderm internalization in *Chironomus* embryos. The gain of Fog and T48 activity during evolution may have allowed *Drosophila* embryos to increase the efficiency of mesoderm internalization by coupling apical constriction with an evolutionarily more ancient, ectodermal compression dependent mechanism.

Actomyosin contractility provides a common force generation mechanism in development. To date, the studies of tissue mechanics have been largely focused on the mechanisms that generate contractile forces that actively deform the tissues[4,58,59]. It remains less well understood how the "passive" mechanical status of the tissue influences the outcome of tissue deformation. The Opto-Rho1DN optogenetic tool developed in this work provides an effective approach to acutely disrupt the myosin-dependent force generation machinery, and therefore can help us begin to discern the role of "active" forces and "passive" mechanical properties in morphogenesis.

Furthermore, our work provides an example for the cooperation between “local”, tissue-autonomous active force production and “global”, tissue-nonautonomous mechanical contribution in tissue morphogenesis. It will be interesting to explore whether such cooperation plays a role in other cell sheet folding processes and whether mechanisms other than apical constriction can be employed to trigger folding in a compressed cell sheet.

Acknowledgements:

We thank members of the He lab and the Griffin lab at Dartmouth College for sharing valuable thoughts during this work; James Moseley and Magdalena Bezanilla for providing constructive suggestions and comments on the manuscript; Ann Lavanway for imaging support. We thank the Wieschaus lab and the De Renzis lab for sharing reagents, Oleg Polyakov for sharing the code for the energy minimization-based vertex model, and the Bloomington Drosophila Stock Center for fly stocks. This study is supported by NIGMS ESI-MIRA R35GM128745 and American Cancer Society Institutional Research Grant #IRG –82-003-33 to B.H.. The study used core services supported by STANTO15R0 (CFF RDP), P30-DK117469 (NIDDK P30/DartCF), and P20-GM113132 (bioMT COBRE).

Author Contributions:

H.G. and B.H. designed the study and performed the embryo experiments and H.G. analyzed the data. M.S. developed Opto-Rho1DN. M.S. and B.H. performed initial characterization of the tool. S.H. and B.H. developed the vertex dynamics model and performed the analysis. B.H. modified the energy minimization-based vertex model (Polyakov et al. model) and performed the analysis. H.G. and B.H. wrote the manuscript. All authors contributed to the production of the final version of the manuscript.

Declaration of Interests:

The authors declare no competing interests.

References

1. Martin, A. C. & Goldstein, B. Apical constriction: themes and variations on a cellular mechanism driving morphogenesis. *Development* **141**, 1987–98 (2014).
2. Munjal, A. & Lecuit, T. Actomyosin networks and tissue morphogenesis. *Development* **141**, 1789–93 (2014).
3. Sawyer, J. M. *et al.* Apical constriction: a cell shape change that can drive morphogenesis. *Dev Biol* **341**, 5–19 (2010).
4. Gilmour, D., Rembold, M. & Leptin, M. From morphogen to morphogenesis and back. *Nature* **541**, 311–320 (2017).
5. Martin, A. C. The Physical Mechanisms of Drosophila Gastrulation: Mesoderm and Endoderm Invagination. *Genetics* **214**, 543–560 (2020).
6. Gheisari, E., Aakhte, M. & Müller, H.-A. J. Gastrulation in Drosophila melanogaster: Genetic control, cellular basis and biomechanics. *Mech. Dev.* **163**, 103629 (2020).
7. Leptin, M. & Grunewald, B. Cell shape changes during gastrulation in Drosophila. *Development* **110**, 73–84 (1990).
8. Sweeton, D., Parks, S., Costa, M. & Wieschaus, E. Gastrulation in Drosophila: the formation of the ventral furrow and posterior midgut invaginations. *Development* **112**, 775–89 (1991).
9. Leptin, M. twist and snail as positive and negative regulators during Drosophila mesoderm development. *Genes Dev* **5**, 1568–76 (1991).
10. Parks, S. & Wieschaus, E. The Drosophila gastrulation gene concertina encodes a G alpha-like protein. *Cell* **64**, 447–58 (1991).

11. Costa, M., Wilson, E. T. & Wieschaus, E. A putative cell signal encoded by the folded gastrulation gene coordinates cell shape changes during Drosophila gastrulation. *Cell* **76**, 1075–89 (1994).
12. Kolsch, V., Seher, T., Fernandez-Ballester, G. J., Serrano, L. & Leptin, M. Control of Drosophila gastrulation by apical localization of adherens junctions and RhoGEF2. *Science* **315**, 384–6 (2007).
13. Manning, A. J., Peters, K. A., Peifer, M. & Rogers, S. L. Regulation of epithelial morphogenesis by the G protein-coupled receptor mist and its ligand fog. *Sci Signal* **6**, ra98 (2013).
14. Kerridge, S. *et al.* Modular activation of Rho1 by GPCR signalling imparts polarized myosin II activation during morphogenesis. *Nat Cell Biol* **18**, 261–70 (2016).
15. Barrett, K., Leptin, M. & Settleman, J. The Rho GTPase and a putative RhoGEF mediate a signaling pathway for the cell shape changes in Drosophila gastrulation. *Cell* **91**, 905–15 (1997).
16. Hacker, U. & Perrimon, N. DRhoGEF2 encodes a member of the Dbl family of oncogenes and controls cell shape changes during gastrulation in Drosophila. *Genes Dev* **12**, 274–84 (1998).
17. Nikolaidou, K. K. & Barrett, K. A Rho GTPase signaling pathway is used reiteratively in epithelial folding and potentially selects the outcome of Rho activation. *Curr Biol* **14**, 1822–6 (2004).
18. Dawes-Hoang, R. E. *et al.* folded gastrulation, cell shape change and the control of myosin localization. *Development* **132**, 4165–78 (2005).

19. Martin, A. C., Kaschube, M. & Wieschaus, E. F. Pulsed contractions of an actin-myosin network drive apical constriction. *Nature* **457**, 495–9 (2009).
20. Mason, F. M., Tworoger, M. & Martin, A. C. Apical domain polarization localizes actin-myosin activity to drive ratchet-like apical constriction. *Nat Cell Biol* **15**, 926–36 (2013).
21. Martin, A. C., Gelbart, M., Fernandez-Gonzalez, R., Kaschube, M. & Wieschaus, E. F. Integration of contractile forces during tissue invagination. *J Cell Biol* **188**, 735–49 (2010).
22. Gelbart, M. A. *et al.* Volume conservation principle involved in cell lengthening and nucleus movement during tissue morphogenesis. *Proc Natl Acad Sci U A* **109**, 19298–303 (2012).
23. He, B., Doubrovinski, K., Polyakov, O. & Wieschaus, E. Apical constriction drives tissue-scale hydrodynamic flow to mediate cell elongation. *Nature* **508**, 392–6 (2014).
24. Polyakov, O. *et al.* Passive mechanical forces control cell-shape change during Drosophila ventral furrow formation. *Biophys J* **107**, 998–1010 (2014).
25. Rauzi, M. *et al.* Embryo-scale tissue mechanics during Drosophila gastrulation movements. *Nat Commun* **6**, 8677 (2015).
26. Munoz, J. J., Barrett, K. & Miodownik, M. A deformation gradient decomposition method for the analysis of the mechanics of morphogenesis. *J Biomech* **40**, 1372–80 (2007).
27. Conte, V., Munoz, J. J., Baum, B. & Miodownik, M. Robust mechanisms of ventral furrow invagination require the combination of cellular shape changes. *Phys Biol* **6**, 016010 (2009).
28. Allena, R., Mouronval, A. S. & Aubry, D. Simulation of multiple morphogenetic movements in the Drosophila embryo by a single 3D finite element model. *J Mech Behav Biomed Mater* **3**, 313–23 (2010).
29. Brodland, G. W. *et al.* Video force microscopy reveals the mechanics of ventral furrow invagination in Drosophila. *Proc Natl Acad Sci U A* **107**, 22111–6 (2010).

30. Etienne-Manneville, S. & Hall, A. Rho GTPases in cell biology. *Nature* **420**, 629–635 (2002).

31. Sebti, S. M. & Der, C. J. Searching for the elusive targets of farnesyltransferase inhibitors. *Nat. Rev. Cancer* **3**, 945–951 (2003).

32. Roberts, P. J. *et al.* Rho Family GTPase Modification and Dependence on CAAX Motif-signaled Posttranslational Modification*. *J. Biol. Chem.* **283**, 25150–25163 (2008).

33. Feig, L. A. & Cooper, G. M. Inhibition of NIH 3T3 cell proliferation by a mutant ras protein with preferential affinity for GDP. *Mol. Cell. Biol.* **8**, 3235–3243 (1988).

34. Liu, H. *et al.* Photoexcited CRY2 interacts with CIB1 to regulate transcription and floral initiation in Arabidopsis. *Science* **322**, 1535–1539 (2008).

35. Kennedy, M. J. *et al.* Rapid blue-light-mediated induction of protein interactions in living cells. *Nat. Methods* **7**, 973–975 (2010).

36. Guglielmi, G., Barry, J. D., Huber, W. & De Renzis, S. An Optogenetic Method to Modulate Cell Contractility during Tissue Morphogenesis. *Dev Cell* **35**, 646–60 (2015).

37. Magie, C. R., Meyer, M. R., Gorsuch, M. S. & Parkhurst, S. M. Mutations in the Rho1 small GTPase disrupt morphogenesis and segmentation during early Drosophila development. *Dev. Camb. Engl.* **126**, 5353–5364 (1999).

38. Johndrow, J. E., Magie, C. R. & Parkhurst, S. M. Rho GTPase function in flies: insights from a developmental and organismal perspective. *Biochem. Cell Biol. Biochim. Biol. Cell.* **82**, 643–657 (2004).

39. Munjal, A., Philippe, J. M., Munro, E. & Lecuit, T. A self-organized biomechanical network drives shape changes during tissue morphogenesis. *Nature* **524**, 351–5 (2015).

40. Coravos, J. S. & Martin, A. C. Apical Sarcomere-like Actomyosin Contracts Nonmuscle Drosophila Epithelial Cells. *Dev. Cell* **39**, 346–358 (2016).

41. Fox, D. T. *et al.* Rho1 regulates Drosophila adherens junctions independently of p120ctn. *Development* **132**, 4819–4831 (2005).

42. Simoes Sde, M. *et al.* Rho-kinase directs Bazooka/Par-3 planar polarity during Drosophila axis elongation. *Dev Cell* **19**, 377–88 (2010).

43. Levayer, R., Pelissier-Monier, A. & Lecuit, T. Spatial regulation of Dia and Myosin-II by RhoGEF2 controls initiation of E-cadherin endocytosis during epithelial morphogenesis. *Nat. Cell Biol.* **13**, 529–540 (2011).

44. Homem, C. C. F. & Peifer, M. Diaphanous regulates myosin and adherens junctions to control cell contractility and protrusive behavior during morphogenesis. *Development* **135**, 1005–1018 (2008).

45. Conte, V. *et al.* A biomechanical analysis of ventral furrow formation in the Drosophila melanogaster embryo. *PLoS One* **7**, e34473 (2012).

46. Gracia, M. *et al.* Mechanical impact of epithelial-mesenchymal transition on epithelial morphogenesis in Drosophila. *Nat. Commun.* **10**, 2951 (2019).

47. Jin Qiu, Lang, J. H. & Slocum, A. H. A curved-beam bistable mechanism. *J. Microelectromechanical Syst.* **13**, 137–146 (2004).

48. Foe, V. E. & Alberts, B. M. Studies of nuclear and cytoplasmic behaviour during the five mitotic cycles that precede gastrulation in Drosophila embryogenesis. *J Cell Sci* **61**, 31–70 (1983).

49. Edgar, B. A., Lehman, D. A. & O'Farrell, P. H. Transcriptional regulation of string (cdc25): a link between developmental programming and the cell cycle. *Dev. Camb. Engl.* **120**, 3131–3143 (1994).
50. Nelson, C. M. On Buckling Morphogenesis. *J. Biomech. Eng.* **138**, 021005 (2016).
51. Gomez, M., Moulton, D. E. & Vella, D. Dynamics of viscoelastic snap-through. *J. Mech. Phys. Solids* **124**, 781–813 (2019).
52. Mazumdar, A. & Mazumdar, M. How one becomes many: blastoderm cellularization in Drosophila melanogaster. *Bioessays* **24**, 1012–22 (2002).
53. Yevick, H. G., Miller, P. W., Dunkel, J. & Martin, A. C. Structural Redundancy in Supracellular Actomyosin Networks Enables Robust Tissue Folding. *Dev. Cell* **50**, 586-598.e3 (2019).
54. Wolpert, L., Tickle, C. & Arias, A. M. *Principles of Development*. (Oxford University Press, 2015).
55. Mao, Y. & Baum, B. Tug of war--the influence of opposing physical forces on epithelial cell morphology. *Dev. Biol.* **401**, 92–102 (2015).
56. Rich, A., Fehon, R. G. & Glotzer, M. Rho1 activation recapitulates early gastrulation events in the ventral, but not dorsal, epithelium of Drosophila embryos. *eLife* **9**, (2020).
57. Urbansky, S., González Avalos, P., Wosch, M. & Lemke, S. Folded gastrulation and T48 drive the evolution of coordinated mesoderm internalization in flies. *eLife* **5**,.
58. Heisenberg, C.-P. & Bellaïche, Y. Forces in tissue morphogenesis and patterning. *Cell* **153**, 948–962 (2013).
59. Chanet, S. & Martin, A. C. Mechanical force sensing in tissues. *Prog Mol Biol Transl Sci* **126**, 317–52 (2014).

Materials and Methods

Generation of CRY2-Rho1DN construct

To generate the CRY2-mCherry-Rho1DN fusion gene, the Rho1 CDS bearing an ACT to AAT mutation and a TGC to TAC mutation (T19N and C189Y, respectively) was synthesized and inserted to the C-terminal end of pCRY2PHR-mCherryN1 (Addgene, deposited by Chandra Tucker) through Gibson assembly. A 12-aa flexible linker sequence (GGGGSGGGGSGG) was included between the mCherry and Rho1DN sequences. The resulting CRY2PHR-mCherry-Rho1N18Y189 fusion gene was subsequently inserted into pTiger, a transformation vector containing the attB site and 14 upstream UAS GAL4-binding sites (courtesy of S. Ferguson, State University of New York at Fredonia, Fredonia, NY, USA). The resulting pTiger-CRY2-mCherry-Rho1DN construct was sent to Genetic Services for integration into the attP2 site using the phiC31 integrase system[60].

Fly stocks and genetics

Fly lines containing the following fluorescent markers were used: *Sqh-GFP*[61], *Sqh-mCherry*[19] and *E-cadherin-GFP*[62].

Fly lines containing *CIBN-pm-GFP (II), CIBN-pm (I)*[36] or *CRY2-Rho1DN (III)* (this study, note that *CRY2-Rho1DN* also contains the *mCherry* tag) were used to generate the following stocks: *CIBN-pm-GFP; CRY2-Rho1DN* and *CIBN-pm; CRY2-Rho1DN*. To generate embryos containing maternally deposited CIBN-pm-GFP and CRY2-Rho1DN proteins, *CIBN-pm-GFP; CRY2-Rho1DN* females were crossed to males from the *Maternal-Tubulin-Gal4* line 67.15 to generate *CIBN-pm-GFP/67; CRY2-Rho1DN/15* females ("*67*" and "*15*" refer to *Maternal-Tubulin-Gal4*

on chromosome II and III, respectively[63]). To generate embryos containing maternally deposited CIBN-pm (without GFP) and CRY2-Rho1DN proteins, *CIBN-pm; CRY2-Rho1DN* females were crossed to *67.15* males to generate *CIBN-pm/+; +/67; CRY2-Rho1DN/15* females. In both cases, embryos derived from the F1 females were used in the optogenetic experiments. The use of CIBN-pm without a GFP tag was to allow better visualization of GFP-tagged myosin regulatory light chain Sqh. The following *Maternal-Tubulin-Gal4* lines were used: (1) *67; 15*, (2) *67 Sqh-mCherry; 15 Sqh-GFP*, (3) *67 Sqh-mCherry; 15 E-cadherin-GFP*, (4) *67 Sqh-GFP; 15* and (5) *67 Sqh-GFP; 15 Sqh-GFP*. Specifically:

- Figure 1c, d, and g, Supplementary Figure 1: *CIBN-pm-GFP; CRY2-Rho1DN* females were crossed to *67; 15* males.
- Figure 1f: *CIBN-pm; CRY2-Rho1DN* females were crossed to *67 Sqh-GFP; 15* males.
- Figure 2, Supplementary Figure 2, 3, 5a, 5c and 5d, Supplementary Figure 6 and 7: *CIBN-pm-GFP; CRY2-Rho1DN* females were crossed to *67 Sqh-mCherry; 15 Sqh-GFP* males.
- Supplementary Figure 4a: *CIBN-pm; CRY2-Rho1DN* females were crossed to *67 Sqh-mCherry; 15 Sqh-GFP* males.
- Supplementary Figure 4c: *CIBN-pm; CRY2-Rho1DN* females were crossed to *67 Sqh-GFP; 15 Sqh-GFP* males.

To generate embryos with *zip* knockdown, *UAS-shRNA-zip* (BL 37480) females were crossed to *67; spider–GFP* males to generate *UAS-shRNA-zip/67; spider–GFP/+* females. Embryos derived from such females were used as *zip* knockdown mutants (*zip-RNAi*).

Viability test for Opto-Rho1DN embryos

Embryo viability test was performed by hand selecting cellularizing embryos derived from *67/CIBNpm-GFP; 15/CRY2-Rho1DN* female flies in a dark room where the only illuminating light is red light. The selected embryos were randomly divided into two groups and placed on two fresh apple juice plates. One plate was kept in dark and the other was placed under a beam of white light with moderate intensity. Plates were kept at 18 °C for more than 48 hours, after which the hatched and unhatched embryos were counted using a Nikon stereo microscope. Three independent trails were conducted. In total, 60 out of 70 stimulated embryos did not hatch whereas all 63 unstimulated embryos hatched.

Live imaging and optogenetic stimulation

To prepare embryos for live imaging, embryos were manually staged and collected from apple juice plates, and dechorionated with ~3% bleach in a dark room using an upright Nikon stereo microscope. In optogenetic experiments, embryos were protected from unwanted stimulation using an orange-red light filter placed on top of white light coming from the stereo microscope. After dechorionation, embryos were rinsed thoroughly with water, and transferred on a 35 mm glass-bottom dish (MatTek Corporation). Distilled water was then added to the dish well to completely cover the embryos. Live imaging was performed in water at room temperature with one of the following approaches.

To examine the plasma membrane recruitment of CRY2-Rho1DN and its impact on cortical association of myosin (Figure 1c-f), embryos were imaged using a Nikon inverted spinning disk confocal microscope equipped with the perfect focus system and Andor W1 dual camera, dual

spinning disk module. An CFI Plan Apo Lambda 60×/1.40 WD 0.13 mm oil objective lens was used for imaging. For membrane recruitment of CRY2-Rho1DN, time lapse movies were taken for post-cellularization embryos at a single z-plane close to the apical side of the tissue at a frame rate of 0.46 s per frame. For cortical association of myosin, a small z-stack (5 slices, 0.5 μm step size) were taken at a rate of 3.46 s per stack. The image size is 858 by 1536 pixels with a lateral pixel size of 0.11 μm, which corresponds to a 94-μm by 169-μm region. For each embryo, pre-stimulation images were acquired using a 561-nm laser, which did not activate Opto-Rho1DN. Stimulation and post-stimulation imaging were performed simultaneously as we subsequently imaged the embryo with both 488-nm and 561-nm lasers in an alternating pattern using triggered excitation.

To examine the spatial confinement of stimulation (Figure 1g) and the effect of activation of Opto-Rho1DN on apical constriction during ventral furrow formation (Supplementary Figure 1), embryos were imaged on a Leica SP5 confocal microscope with a 63×/1.3 NA glycerin-immersion objective lens. A 2× zoom was used. 20 confocal z-sections with a step size of 1 μm were acquired every 13 s. The image size is 1024×512 pixels with a lateral pixel size of 240 nm. The total imaged volume is approximately 246×123×19 μm. First, a single-time-point pre-stimulated image stack was acquired using a 561-nm laser. Next, stimulation was performed by taking a single-time-point image stack using both 488-nm and 561-nm lasers, which took 13 s. Stimulation was followed by post-stimulation acquisition with 561-nm laser for 20 time points (260 s). The stimulation and post-stimulation acquisition cycle was repeated until the end of the movie (i.e., stimulated for 13 s every 273 s).

To examine the stage-specific effect of Opto-Rho1DN activation on ventral furrow invagination (Figure 2), embryos were imaged on an Olympus FVMPE-RS multiphoton system equipped with a 25×/1.05 numerical aperture water immersion objective lens. Pre-stimulation images were obtained by using a 1040-nm laser to excite a region of interest (260×512) under 3× digital zoom. Continuous imaging was conducted for pre-stimulation imaging. For each time point, a 100-μm z-stack with step size of 1μm was obtained with linearly increased laser intensity (4%-7.5%) over Z, which took 34 s. Stimulation was performed at different stages of ventral furrow formation using a 458-nm single-photon diode laser by illuminating the whole embryo under 1× digital zoom for 12 s with 0.3% laser intensity. A wait period of ~ 20 s was imposed after stimulation. Post-stimulation images were obtained using both 1040-nm and 920-nm lasers. Same setting as pre-stimulation imaging was applied, with an addition of a linear increase in 920-nm laser intensity (0.1%-0.5%) over Z. Stimulation was conducted manually every 5 stacks during post-stimulation imaging (i.e., stimulation for 12 s every ~200 s) to ensure the sustained membrane recruitment of CRY2-Rho1DN.

To examine ventral furrow invagination in *zip RNAi* embryos expressing Spider-GFP (Supplementary Figure 10), deep tissue live imaging was performed with a custom-built two-photon scanning microscope built around an upright Olympus BX51 [22]. Fluorescence emissions were collected both through an Olympus 40× NA0.8 LUMPlanFl/IR water immersion objective lens) and through an NA1.3 oil condenser lens and were detected with high quantum efficiency GaAsP photomultipliers (Hamamatsu). The microscope was operated by the MATLAB software ScanImage modified to control a piezo objective (PI) and to allow laser power to be increased with greater imaging depth. Images were taken with an excitation wavelength of 920-nm under

3× digital zoom. Stacks of 40 images taken at 2-μm steps were recorded every 8 s. Each image is 256 pixels×128 pixels (~0.6 μm/pixel), corresponding to a 150 μm (medial–lateral) ×75 μm (anterior–posterior) region. The imaged regions are approximately centered at the ventral midline.

Detecting ectodermal compression by laser microdissection

Embryos expressing E-cadherin-GFP were prepared in the same way as in regular live imaging described above. The embryos were mounted on the coverslip with an orientation that the lateral ectoderm at one side of the embryo was facing the objective. Single color imaging was performed using an Olympus FVMPE-RS multiphoton microscope equipped with a 25×/1.05 numerical aperture water-immersion objective and a 920 nm pulsed laser. A 3× zoom was used. For each embryo, a stack of 51 images taken at 2-μm steps were acquired before the treatment to determine the stage of the embryo. These images encompass the middle portion of the embryo between the anterior and posterior poles and are 512×128 pixels (170×42 μm) in size. To record the response of the tissue immediately before and after laser ablation, time lapse movies at a single focal plane ~17 μm deep from the surface of the embryo (approximately at the middle of the cell's apical-basal axis) were acquired at a frame rate of 0.93 frame per second. To perform laser cutting, a rectangle region of interest (ROI) approximately 100×160 pixels (33×53 μm) in size covering approximately 5×9 cells was subjected to laser scanning with an increased laser power. The scanning was performed continuously across at a series of z positions from 9 to 27 μm deep from the surface with a step size of 2 μm. The scanning of the entire volume, which covers the middle third of the apical basal axis of the cells, took approximately 3 seconds. The laser intensity was finetuned such that the laser did not generate damage to the cell membrane (as

evidenced by the recovery of the membrane signal one minute after laser microdissection) but could impair the mechanical integrity of the cells (as evidenced by the retraction of surrounding tissues when cutting was performed in regions that are under tension).

Disrupting cellularization of lateral ectodermal cells by laser ablation

Disruption of cellularization of the lateral ectodermal cells was carried out on an Olympus FVMPE-RS multiphoton microscope equipped with a 25×/1.05 numerical aperture water-immersion objective and a 920 nm pulsed laser. A 2× digital zoom was used. Embryos at early cellularization stage were mounted on a glass bottom dish with their ventral side facing the objective. First, we focused at a plane in the embryo 60 μm away from the ventral surface. At each lateral side of the embryo, the cellularization front of the ectodermal cells was clearly visible as a line parallel to the surface with a few micrometers' distance from the surface. Ablation of the cellularization front was performed on both sides of the embryo by scanning a high intensity laser beam across a narrow region below the surface that covers the cellularization front. The same approach was then repeated at a series of z planes from 60 μm to 110 μm, with a step size of approximately 10 μm. After ablation, image stacks (101 z-sections, step size = 1 μm) were acquired under 2× digital zoom every 40 seconds. The image size was 512×128 pixels with a pixel size of 0.5 μm. The total imaged volume is approximately 256×64×100 μm^3.

Image analysis and quantification

All image processing and analysis were processed using MATLAB (The MathWorks) and ImageJ (NIH).

To quantify the percent membrane recruitment of CRY2-Rho1DN after stimulation (Figure 1d), cell membrane was segmented based on the CIBN-pm-GFP signal using a custom MATLAB code. The resulting membrane mask was used to determine the signal intensity of CRY2-Rho1DN (mCherry tagged) along the cell membrane over time. The intensity of the CRY2-Rho1DN signal in the cytoplasm, which is determined as the average intensity in the cells before stimulation, was subtracted from the measured intensity. The resulting net membrane signal intensity was further normalized by scaling between 0 and 1.

The invagination depth D (i.e., the distance between the vitelline membrane and the apex of the ventral-most cell, e.g., Figure 2b) and the apical-basal length of the ventral cells over the course of ventral furrow formation (Supplementary Figure 2a, b) were manually measured from the cross-section view of the embryos using ImageJ.

To categorize embryo responses to stage-specific Opto-Rho1DN stimulation, first, each post-stimulation movie was aligned to a representative control movie based on the intermediate furrow morphology at the time of stimulation. The resulting aligned time was used in the analysis because it provided a better measure of the stage of ventral furrow formation than the "absolute" time defined by the onset of gastrulation in each embryo. Next, dD/dt immediately after stimulation are determined by a linear fitting of D over time in the first 4 minutes after stimulation (Supplementary Figure 2f). Embryos with $dD/dt < -0.3$ μm/min are defined as Early Group. These embryos undergo tissue relaxation and result in decrease in D over time. Embryos with dD/dt between -0.3 μm/min and 0.3 μm/min are defined as Mid Group. These embryos do not undergo obvious tissue relaxation but display a temporary pause before they continue to

invaginate. Embryos with $dD/dt > 0.3$ μm/min are defined as Late Group. These embryos continue to invaginate despite the rapid inactivation of myosin. To quantify the impact of myosin inhibition on furrow invagination (Figure 2d), the delay time in furrow invagination (T_{delay}) was measured. T_{delay} is defined as the difference in time for a given stimulated embryo to reach a D of 20 μm compared to a representative control embryo.

To examine the change of apical cell area of the flanking, non-constricting cells in stimulated Opto-Rho1DN embryos (Supplementary Figure 3a, b), a custom MATLAB script was used to generate a flattened surface view of the embryo which accounts for the curvature of the embryo. The apical cell area was measured by manually tracking and outlining flanking cells followed by area measurement using ImageJ.

To measure ectodermal shortening (Supplementary Figure 7), the thickness of the lateral ectoderm is reported as the cross-section area of the ectodermal cell layer between 60° and 90° from the dorsal-ventral axis, which provides a good readout of tissue volume redistribution in 3D. A custom MATLAB script was used to facilitate the measurement. Specifically, the apical surface of the tissue was determined by automatic segmentation of the vitelline membrane of the embryo. The resulting curve was subsequently fit into a circle ("the outer membrane circle"). The basal surface of the tissue was determined by automatic segmentation and tracking of the basal myosin signal, with necessary manual corrections when the basal signal became too dim to be segmented accurately. Tissue thickness was measured as the cross-section area of a section of the ectodermal tissue bounded by the outer membrane, the basal surface, and two radii of the outer membrane circle that are 60° and 90° away from the ventral midline, respectively.

To measure the ectodermal compression, we examined the shape of the laser treated region over time by tracking the surrounding intact cells before and after laser dissection. Cell membrane was segmented based on the E-cadherin-GFP signal using EDGE, a MATLAB-based cell segmentation tool [22]. The two columns of untreated cells immediately next to the medial (proximal to the ventral midline) and lateral (distal to the ventral midline) boundaries of the treated region, respectively, were tracked over time. The change in the average width between these two columns of cells (i.e., the width of the treated region along the medial-lateral axis) over time was used to refer tissue expansion or shrinking after microdissection. For each embryo, a non-treated region more anterior or posterior to the microdissected region was measured in the same way as a control. The average rate of change in width within 10 seconds immediately before microdissection ("Pre-treatment") or within 15 seconds immediately after microdissection ("Post-treatment") was calculated and compared between groups.

To measure ectodermal cell movement in wildtype embryos during ventral furrow formation (Figure 5b, c), the EDGE program was used to segment the cell outlines from the surface views and to determine the position of the centroid of the segmented cells over time.

To detect ectodermal cell movement in Early Group embryos after stimulation (Supplementary Figure 6), kymographs were generated from the surface views with the CIBN-pmGFP signal that marks the cell membrane. Individual membrane traces within the first six minutes after stimulation were manually tracked from the kymograph using the line selection tool in ImageJ. The slope of the lines was subsequently measured using ImageJ to calculate the rate of

membrane movement, which was then plotted against the position of corresponding membrane relative to the ventral midline at the time of stimulation. The average velocity of tissue movement at ventral mesodermal (from -10 to -40 μm and from 10 to 40 μm) or lateral ectodermal (from -60 to -120 μm and from 60 to 120 μm) regions of the embryos was calculated and tested using one-tailed one-sample t-test against 0.

To measure the apical constriction rate in the ectodermal ablation experiment (Figure 6c), kymographs were generated from the surface views with the cell membrane signal (E-cadherin-GFP) to visualize apical constriction and cell movement over time. An approximately 10-cell wide region that is within the constricting domain and centered at the ventral midline was selected. The width change of the selected region was tracked on the kymograph from the onset of gastrulation to indicate the progress of apical constriction. Similar measurements of apical constriction rate were performed for the *zip RNAi* and control embryos (Supplementary Figure 10).

Energy minimization-based vertex model for ventral furrow formation (Polyakov et al model)

The 2D vertex model for ventral furrow formation, which considers the cross-section view of the embryo, was constructed as previously described[24]. In brief, the model contains a ring of 80 cells that represent the cross-section of an actual embryo. The initial geometry of the cells in the model resembles that in the real embryo. The apical, basal and lateral membranes of the cells are modeled as elastic springs that resist deformation, and the cells have a propensity to remain constant cell volume (area in 2D). In the model, apical constriction provides the sole driving

force for tissue deformation, which is achieved by allowing the apex of the cells in the ventral region of the embryo to shrink. The resulting morphological changes of the tissue are determined by the stiffness of the apical, lateral, and basal springs, cell volume conservation, and a stepwise reduction of basal spring stiffness (see below).

The energy equation that approximates the mechanical properties of the system is described by the following expression:

$$E = \sum_i \varphi_i \mu_i a_i^2 + \sum_i [k_l (l_i - l_0)^2 + k_b (b_i - b_0)^2 + k_a (a_i - a_0)^2]$$

$$+ \sum_i C_{VOL}(V_i) + C_{YOLK}(V_{yolk})$$

The first term in the equation stands for myosin mediated apical constriction. The term $\varphi_i \mu_i$ defines the spatial distribution of myosin contractility. φ_i equals to 1 for cells within the mesoderm domain (9 cells on each side of the ventral midline, a total of 18 cells) and 0 for the rest of cells, which ensures that only the mesodermal cells will constrict apically. μ_i is a Gaussian function that peaks at the ventral midline. Specifically,

$$\mu_i = \mu_0 e^{\frac{(i - i_{mid})^2}{2\sigma^2}}$$

Here i_{mid} stands for the cell ID at the ventral midline, μ_0 defines the strength of apical constriction and σ defines the width of the force distribution. Note that due to the Gaussian-shaped force distribution, only 12 cells at the ventral most region of the embryo will undergo apical constriction, similar to what occurs in the real embryo.

The second term in the equation stands for the elastic resistance of the membranes. a_i, b_i, and l_i stand for the area (length in 2D) of the apical, basal and lateral membrane of cell i, respectively.

a_0, b_0, and l_0 are the corresponding resting length, which are set to be their initial length. k_a, k_b and k_l are the spring constant of the apical, basal and lateral springs, respectively.

The third and fourth terms, C_{VOL} and C_{YOLK}, are constraint functions that describe volume conservation of the cells and the yolk, respectively. These two terms impose penalties when the volume deviates from the resting value. Specifically,

$$C_{VOL}(V_i) = K_v(V_i - V_0)^2$$

$$C_{YOLK}(V_{yolk}) = K_Y(V_{yolk} - V_{0,yolk})^2$$

Here, V_i stands for the volume of cell i. V_0 stands for the initial equilibrium volume of cell i. Similarly, V_{yolk} stands for the volume of the yolk. $V_{0,yolk}$ stands for the initial equilibrium volume of the yolk. K_v and K_{yolk} control the deviation of the cell volume and the yolk volume from the initial equilibrium values, respectively.

In the simulation, the basal rigidity of the epithelium (k_b) decreases adiabatically, allowing the model to transition through a series of intermediate equilibrium states defined by the specific k_b values. These intermediate states recapitulate the lengthening-shortening dynamics of the constricting cells observed in the real embryos [24].

To produce an in-plane compressive stress in the ectodermal tissue, we set the resting length of the lateral springs (l_0) 20% shorter than their original length. Because of the cell volume conservation constraint, shortening of the ectodermal cells in the apical-basal direction will result in an expansion of cells in the orthogonal direction, which is the planar direction of the epithelium. This expansion provides a mechanism to produce in-plane compressive stress in the

epithelial sheet. To simulate the optogenetic inhibition of myosin contractility in the model, we set the program such that the apical contractility term will be reduced to zero at defined intermediate equilibrium state. This approach allows us to inhibit apical contractility at any intermediate furrow configuration specified by k_b.

In order to simulate the impact of impairing apical constriction on invagination, we modified our model in two different ways. First, to reduce the number of apically constricting cells, we decreased the width of the Gaussian function that defines the spatial distribution of apical myosin contractility. Second, to recapitulate the weakened and uncoordinated apical constriction observed in certain apical constriction mutants, we inhibited apical constriction from every other cell within the ventral 18-cell region.

List of parameters used in Figure 3c:

Parameter	***Value***
k_a	30
k_l	20
k_b*	$2^{10} \rightarrow 2^9 \rightarrow 2^8 \rightarrow 2^7 \rightarrow 2^6 \rightarrow 2^5 \rightarrow 2^4 \rightarrow 2^3 \rightarrow 2^2 \rightarrow 2^1 \rightarrow 2^0$
μ_0	5000
σ	3
K_v	5000
K_Y	1

*: In the simulation, k_b decreases adiabatically from 2^{10} to 2^0.

Vertex dynamics model on epithelial buckling

1. Overview

This 2D vertex dynamics model is designed to investigate the dynamics of an elastic sheet undergoing spatially confined apical constriction in the presence or absence of in-plane

compression. The elastic monolayer is composed of 160 equal-size square-shaped units ("cells") confined in a circular shell, resembling the 2-dimentioal cross-section of an elastic tube (Figure 5d). Each cell comprises of an apical edge, a basal edge and two lateral edges ("membranes"), connected by nodes ("vertices"). Each lateral membrane is shared between two neighboring cells, reflecting cell adhesion-mediated tight mechanical coupling of adjacent lateral membranes. The initial length of the edges is approximately 4% of the radius of the elastic ring. The edges of cells are elastic and can resist stretching and compression like springs. The inner space of each cell resists volume changes, resembling the behavior of an incompressible cytoplasm. A weak torsion spring is implemented at each corner of the cell to prevent unlimited shear deformations. The model is driven out of the initial equilibrium configuration by spatially confined apical constriction within designated group of cells. Cells outside of the constriction region could generate in-plane compressive stresses by moderately constricting their lateral edges. For convenience, we refer to the region of the monolayer where apical constriction occurs as the mesoderm and the region outside of the constriction domain as the ectoderm. The forces exerted on each vertex are integrated and used to determine the movement of the vertex within short time intervals, mediating the stepwise evolution of the model.

2. Passive components of the model

The passive components of the model (i.e., the mechanical properties of the elastic ring) are determined by the following mechanisms:

(2a) Elastic forces of the cell membranes. The apical, basal and lateral cell membranes are elastic and can resist changes in their area (edge length in the 2D model). To implement this property in

906 the model, we consider the adjacent nodes as being connected by springs. When the distance
907 between two adjacent nodes deviates from the resting length of the spring, a restoring force will
908 be applied on the nodes:

909 $$F_{ij}^{e} = -k_e\left(l_{ij} - l_0\right)$$

910 Here F_{ij}^{e} denotes the elastic force between node i and j . k_e is the elastic constant. l_{ij} and l_0
911 represent the current and the equilibrium distance (i.e., the length of the edge/spring) between
912 node i and j. l_0 is set to be equal to the initial edge length.

913

914 *(2b) Resistance to cell volume changes*. The cells in the model have a propensity to maintain
915 their volume (cell area in the 2D model). To implement this mechanism, when the cell volume
916 deviates from the equilibrium level, inward- or outward-pointed forces are applied on all nodes
917 of the cell attempting to restore the cell volume to the equilibrium level in a way analogous to
918 osmotic pressure (Supplementary Figure 8a). The volume restoration force F_i^v applied on each
919 node of cell i is determined by the difference between the cell volume V_i and the equilibrium
920 volume V_0:

921 $$F_i^v = -k_v(V_i - V_0)$$

922 k_v is the constant for the volume restoration force. In the simulation, k_v is specified such that the
923 cell area changes do not exceed 10% of the original level.

924

925 *(2c) Resistance to shear*. In order to constrain the shear deformation of the cell, we implemented
926 corner stiffness by creating a torch ("shear resistance force") between each pair of connected
927 membranes in a cell to resist changes in angle between these membranes.

928 $$F_i^s = -k_s(\theta - \pi/2)$$

929 The shear resistance force F_i^s is related to the angle (θ, in radian) between the two membranes
930 connected through the node i. When θ deviates from $\pi/2$, a force will be applied to node i
931 attempting to restore θ to $\pi/2$ (Supplementary Figure 8b).
932
933 *3. Active components of the model*
934 In addition to the "passive" responsive forces mentioned above, we also implemented "active"
935 forces to drive the deformation of cells. These forces are applied by adding additional springs
936 between neighboring nodes.
937
938 *(3a) Apical constriction.* The first type of active forces is apical constriction of the ventral
939 mesodermal cells. The constriction force is implemented by adding a spring with a shorter
940 equilibrium length between the apical nodes of the cell.
941 $$F_{ij}^{ac} = -k_{ac}(l_{ij} - l_{ac}), \qquad (l_{ac} < l_0)$$
942 Here, an apical constriction force F_{ij}^{ac} is generated between adjacent apical nodes *i* and *j* when
943 the distance between the two nodes (l_{ij}) is larger than the equilibrium length of the apical
944 constriction spring (l_{ac}), which is set as 1/100 of the initial edge size l_0. k_{ac} is the elastic
945 constant of the apical constriction spring. The value of k_{ac} depends on the location of the cell in
946 the elastic ring, as detailed below.
947
948 At any given time, the spatial distribution of k_{ac} is set to follow a quasi-Gaussian distribution
949 encompassing the ventral mesoderm and centered at the ventral midline to reflect the graded
950 distribution of apical myosin in real embryos (Supplementary Figure 8e). For a given cell *i*
951 located at the right half of the circle, starting from the ventral midline, k_{ac} is determined by the

952 following function:

953 $$k_{ac}(i) = \max\left(C_{ac}e^{\left(-\frac{1}{2\sigma^2}\left(\frac{i-1}{N_{ac}}\right)^2\right)} - C_{ac}e^{\left(-\frac{1}{2\sigma^2}\left(\frac{N_{ac}-1}{N_{ac}}\right)\right)}, 0\right)$$

954 The term $C_{ac}e^{\left(-\frac{1}{2\sigma^2}\left(\frac{i-1}{N_{ac}}\right)^2\right)}$ describes the Gaussian distribution of k_{ac}. N_{ac} is the number of
955 constricting cells on each side of the ventral midline, which is set as 16. The constriction
956 constant C_{ac} is set as 2.5. σ defines the spread of the distribution, which is set as 0.51. The term
957 $C_{ac}e^{\left(-\frac{1}{2\sigma^2}\left(\frac{N_{ac}-1}{N_{ac}}\right)\right)}$ is a cutoff value which makes k_{ac} outside of the constricting domain zero. The
958 spatial distribution of k_{ac} at the left half of the circle is a mirror image of the right half.

959

960 In addition, the value of k_{ac} also evolves over time to resemble the gradual accumulation of
961 apical myosin during ventral furrow formation. Specifically, we let k_{ac} to increase from zero to
962 the maximal k_{ac} (k_{ac}^{max}) between timepoints t_{ac1} and t_{ac2}, which are set as 0 and 60,000,
963 respectively (Supplementary Figure 8g, h). k_{ac}^{max} is specified according to the position of the cell
964 as described above. For each cell, the temporal profile of k_{ac} is defined by the following
965 equation:

966 $$k_{ac}(t) = (9f_t^3(10 - 15f_t + 6f_t^2) + 1)k_{ac}^{max}, \text{ where } f_t = \frac{t - t_{ac1}}{t_{ac2} - t_{ac1}}$$

967

968 *(3b) Ectodermal compression.*

969 The second type of active forces is the compressive forces along the planar axis of the monolayer
970 (Supplementary Figure 8f). In our model, ectodermal compression is generated by active
971 shortening of the ectodermal cells along their apical-basal axis, which results in compression in
972 the planar direction due to the propensity of cells to maintain their volume. We implemented this
973 mechanism by adding constricting springs to the lateral sides of the ectodermal cells.

$$F_{ij}^{lc} = -k_{lc}(l_{ij} - l_{lc}), \qquad (l_{lc} < l_0)$$

The ectodermal shortening force F_{ij}^{lc} will be exerted on nodes *i* and *j* at the two ends of the same lateral edge if the length of the edge (l_{ij}) is greater than the equilibrium length of the lateral constriction spring (l_{lc}), which is set to be smaller than the initial lateral edge size l_0. k_{lc} is the elastic constant of the lateral constriction springs.

Similar to k_{ac}, the value of k_{lc} also depends on the location of the cell in the elastic ring, such that only the ectodermal cells will generate in-plane compressive stresses through active apical-basal shortening (Supplementary Figure 8f). For cells located at the right half of the circle, k_{lc} is defined as follows:

$$k_{lc}(i) = \begin{cases} 0, & (1 \leq i < 16) \\ \dfrac{(i-16)}{8} k_{lc}^{max}, & (16 \leq i \leq 24) \\ k_{lc}^{max}, & (24 < i \leq 80) \end{cases}$$

The spatial distribution of k_{lc} at the left half of the circle is a mirror image of the right half.

In order to reflect our experimental observation that the onset of ectodermal compression is several minutes later than the onset of apical constriction, we set the temporal profile of ectodermal compression such that it is only in play after a certain time point. The temporal profile is achieved by allowing l_{lc} to reduce from l_0 to $p_{lc} l_0$ ($0 \leq p_{lc} < 1$) between timepoints t_{lc1} and t_{lc2} (Supplementary Figure 8g). t_{lc1} and t_{lc2} are set as 60,000 and 90,000, respectively.

4. Geometrical constraints and boundary conditions

(4a) Forces that prevent cell overlapping. We implemented forces analogous to Lennard-Jones

995 forces to prevent the cells from overlapping with each other. When any given node becomes too
996 close to an edge/membrane that connects two other nodes, a repulsive force is applied to prevent
997 the node from passing through the membrane (Supplementary Figure 8c).

998 $$F_i^{LJ} = \frac{k_{LJ}}{r_i^3}\left(6\left(\frac{r_0}{r_i}\right)^4 - 8\left(\frac{r_0}{r_i}\right)^2\right)$$

999 For any given pair of membrane and node *i*, the repulsive force F_{LJ} is related to the shortest
1000 distance (r_i) between the node and the membrane. k_{LJ} is a constant for the repulsive force. r_0 is a
1001 normalizing parameter on distance which is set as 2 in the simulation. To enhance the stability of
1002 the simulation, F_i^{LJ} plateaus when r_i is below 0.3.
1003
1004 *(4b) The impenetrable outer shell.* The elastic ring is confined within a non-penetrable and non-
1005 deformable circular boundary that mimics the eggshell of the embryo. When a node moves to the
1006 close vicinity of the outer shell, the node will receive a repulsive force that prevent it from
1007 getting closer to the shell. The force is similar to F_i^{LJ} that prevents cells from overlapping with
1008 each other.
1009
1010 *(4c) Yolk hydrostatic pressure.* To mimic the turgor pressure from the yolk region of the embryo,
1011 we consider that the space enclosed by the elastic ring is filled with fluid that exerts a hydrostatic
1012 pressure on the basal side of the elastic ring. The resulting force exerted on each basal node *i*
1013 (F_i^y) is normal to the basal surface and is outbound (Supplementary Figure 8d).
1014
1015 *5. Dynamics of tissue deformation*
1016 A timer ticks every 100 ms and the nodes move by a certain distance each time the timer ticks.

We consider that the movement occurs in a viscous, low Reynolds number environment where the inertia is negligible [23], and that the forces acting on each node due to the active and passive mechanisms described above are balanced by viscous drag. The rate at which the node moves is governed by the Stoke's law, which is proportional to the viscous drag.

6. Summary of parameters used in Figure 5

Parameter	***Value***
k_a	0.3
k_l	0.3
k_b	0.2
k_{os}	0.45
k_{ac}^{max}	2.09
k_{lc}^{max}	1
p_{lc}	0.4
k_{LJ}	0.001
F^y	0.25

Statistics

Sample sizes for the presented data and methods for statistical comparisons can be found in figure legends. *p* values were calculated using MATLAB ttest2 or ranksum function.

References

60. Groth, A. C., Fish, M., Nusse, R. & Calos, M. P. Construction of transgenic Drosophila by using the site-specific integrase from phage phiC31. *Genetics* **166**, 1775–1782 (2004).
61. Royou, A., Sullivan, W. & Karess, R. Cortical recruitment of nonmuscle myosin II in early syncytial Drosophila embryos: its role in nuclear axial expansion and its regulation by Cdc2 activity. *J Cell Biol* **158**, 127–37 (2002).

62. Oda, H. & Tsukita, S. Real-time imaging of cell-cell adherens junctions reveals that Drosophila mesoderm invagination begins with two phases of apical constriction of cells. *J Cell Sci* **114**, 493–501 (2001).

63. Hunter, C. & Wieschaus, E. Regulated expression of nullo is required for the formation of distinct apical and basal adherens junctions in the Drosophila blastoderm. *J Cell Biol* **150**, 391–401 (2000).

Figure 1

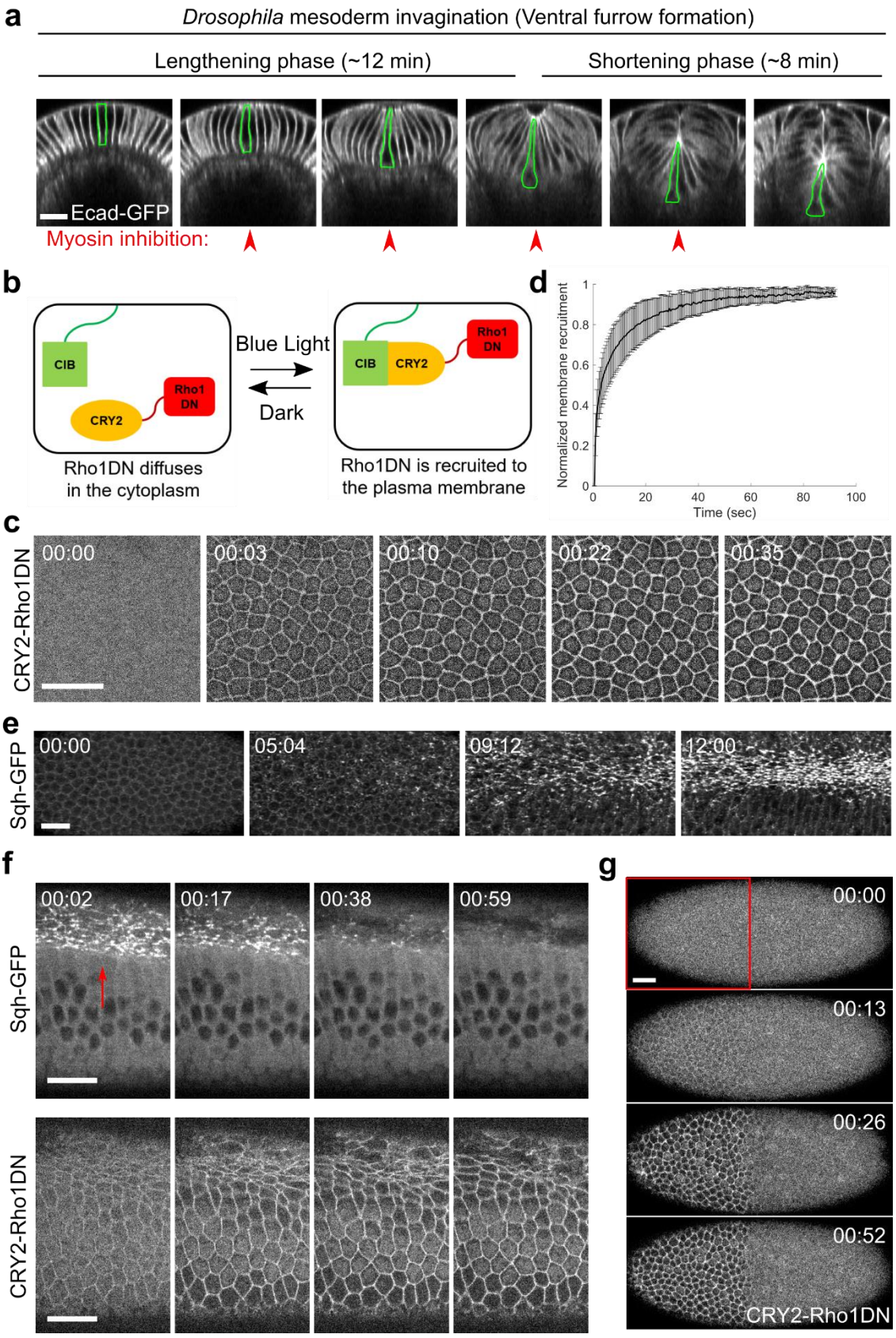
a
Drosophila mesoderm invagination (Ventral furrow formation)
Lengthening phase (~12 min)
Shortening phase (~8 min)
Ecad-GFP
Myosin inhibition:
b
CIB
CRY2
Rho1 DN
Blue Light
Dark
Rho1DN diffuses in the cytoplasm
Rho1DN is recruited to the plasma membrane
d
Normalized membrane recruitment
Time (sec)
c
CRY2-Rho1DN
00:00
00:03
00:10
00:22
00:35
e
Sqh-GFP
00:00
05:04
09:12
12:00
f
Sqh-GFP
00:02
00:17
00:38
00:59
CRY2-Rho1DN
g
00:00
00:13
00:26
00:52
CRY2-Rho1DN

Figure 1. Light-dependent membrane recruitment of CRY2-Rho1DN results in rapid myosin inactivation. (a) *Drosophila* mesoderm invagination occurs in distinct lengthening and shortening phases. Ventral side is up (same for all cross-section images in this work unless otherwise stated). A single ventral cell undergoing apical constriction is outlined in green. In this study, we sought to test whether myosin contractility is required throughout the folding process by acute, stage-specific inhibition of Rho1 (arrow heads). **(b)** Cartoon depicting the principle of the optogenetic tool used in this study. Upon blue light stimulation, CRY2-Rho1DN is translocated from the cytosol to the plasma membrane through the interaction between CRY2 and membrane anchored CIBN. **(c)** Confocal images showing the rapid membrane recruitment of CRY2-Rho1DN upon blue light illumination. **(d)** Relative abundance of membrane recruited CRY2-Rho1DN over time after blue light stimulation. Error bar: s.d., N = 6 embryos. **(e)** A wildtype embryo expressing Sqh-GFP showing apical myosin accumulation during ventral furrow formation. N = 4 embryos. **(f)** Activation of Opto-Rho1DN results in rapid dissociation of myosin from the ventral cell cortex (arrow) in a gastrulating embryo. N = 8 embryos. **(g)** Confocal images showing the confined membrane recruitment of CRY2-Rho1DN within a region of interest (ROI, red box) that has been scanned by a focused beam of blue laser. N = 6 embryos. All scale bars = 20 μm.

Figure 2

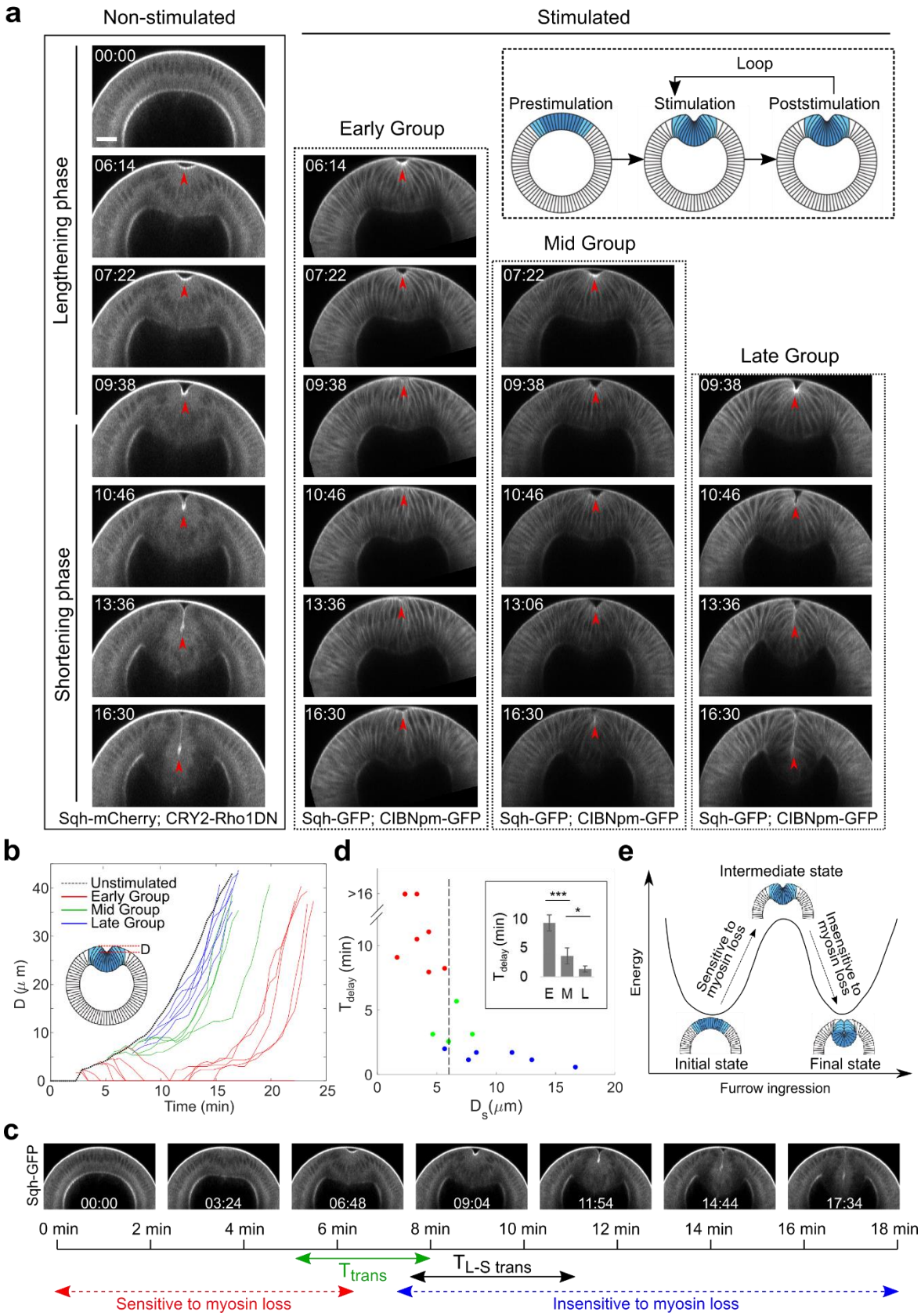
a
Non-stimulated
Stimulated
Lengthening phase
Shortening phase
00:00
06:14
07:22
09:38
10:46
13:36
16:30
Sqh-mCherry; CRY2-Rho1DN
Early Group
Mid Group
Late Group
Sqh-GFP; CIBNpm-GFP
Loop
Prestimulation
Stimulation
Poststimulation
b
Unstimulated
Early Group
Mid Group
Late Group
D (μ m)
Time (min)
d
T_delay (min)
D_s (μm)
E M L
e
Intermediate state
Sensitive to myosin loss
Insensitive to myosin loss
Energy
Initial state
Final state
Furrow ingression
c
Sqh-GFP
00:00
03:24
06:48
09:04
11:54
14:44
17:34
0 min
2 min
4 min
6 min
8 min
10 min
12 min
14 min
16 min
18 min
T_trans
T_L-S trans
Sensitive to myosin loss
Insensitive to myosin loss

Figure 2. Acute inhibition of actomyosin contractility results in stage-dependent response during ventral furrow formation. (a) Still images from multiphoton movies showing different tissue responses to acute loss of myosin contractility during ventral furrow formation. Early Group, Mid Group and Late Group embryos (N = 8, 4, and 6 embryos, respectively) are defined based on their immediate response to myosin inhibition. For stimulated embryos, the first frame corresponds to the time point immediately after stimulation. The inset depicts the stimulation and imaging protocol. Arrowheads indicate the apex of the ventral most cells. **(b)** Time evolution of the invagination depth "D" for the stimulated embryos and a representative unstimulated control embryo. For stimulated embryos, all movies were aligned in time to the representative control embryo based on furrow morphology at the time of stimulation. **(c)** Relationship between the transition phase for sensitivity to myosin inhibition (T_{trans}) and lengthening-shortening transition ($T_{L\text{-}S\ trans}$). **(d)** Scatter plot showing the relation between invagination depth at the time of stimulation (D_s) and the delay time (T_{delay}) in furrow invagination compared to the representative control embryo. T_{delay} is highly sensitive to D_s, with a switch-like change at $D_s \sim 6$ μm (dashed line). Inset: Average T_{delay} in Early (E, n = 5 embryos that invaginated), Mid (M, n = 4) and Late (L, n = 6) Group embryos. *: $p < 0.05$; ***: $p < 0.005$; Student's t-test. **(e)** Cartoon depicting mechanical bistability of the mesoderm during gastrulation. Both the initial, pre-constriction state and the final, fully invaginated state are stable. During gastrulation, actomyosin contractility is critical for bringing the system from the initial state to an intermediate, transitional state, whereas the subsequent transition to the final state can occur independent of myosin contractility.

Figure 3

a

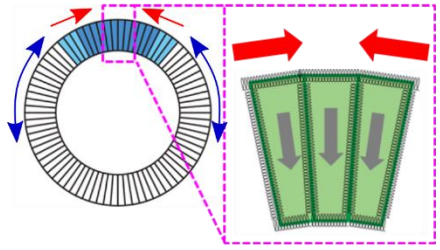

Modified from Polyakov et al., 2014

b

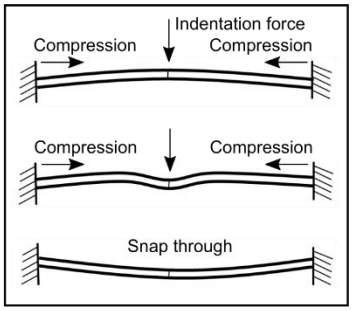

Modified from Qiu et al., 2004

c

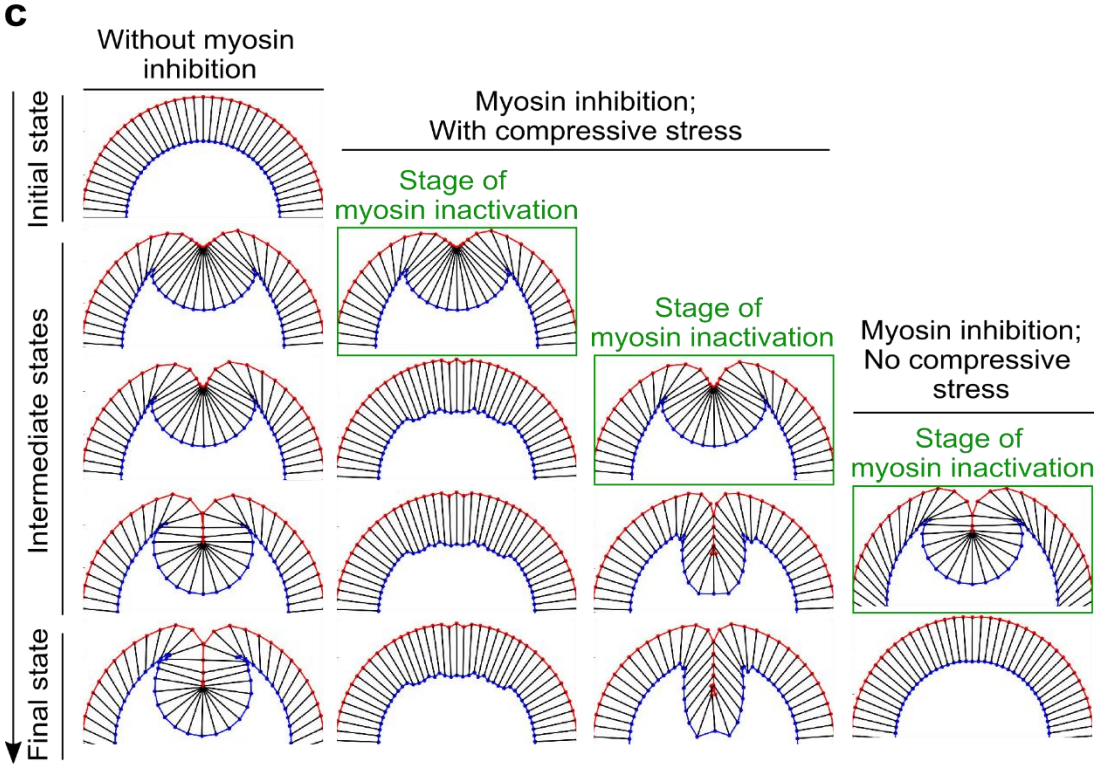

d

Final equilibrium configuration

	No compressive stress	With compressive stress
6 constricting cells (50% of WT)	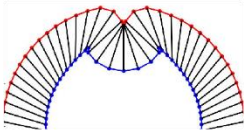	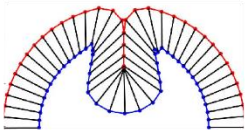
Constriction in every other cell	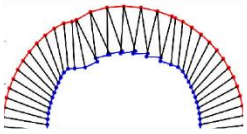	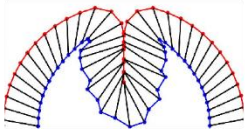

1082

Figure 3. Mechanical bistability of the mesoderm during gastrulation can arise from ectoderm-derived compressive stresses. (a) 2D vertex model testing the mechanisms of mechanical bistability of the mesoderm during gastrulation. In this model, the apical, lateral and basal cortices of cells are modeled as elastic springs that resist deformations, the cell interiors are non-compressible, and the sole active energy inputs are apical constriction in the mesoderm (blue cells) and in-plane compression generated by the ectoderm (white cells). **(b)** Buckling of a compressed elastic beam triggered by a transverse indentation force. **(c)** The model recapitulates the bipartite response to acute loss of actomyosin contractility only when the in-plane compression is present. Column 1 shows normal ventral furrow formation. Column 2 – 4 show tissue response when apical constriction is inhibited at different stages of ventral furrow formation with or without ectodermal compression. **(d)** Model predictions on the impact of reducing the width of apical constriction domain or the uniformity of apical constriction on final invagination depth. In the presence of compressive stress, final invagination depth becomes less sensitive to perturbations of apical constriction.

Figure 4

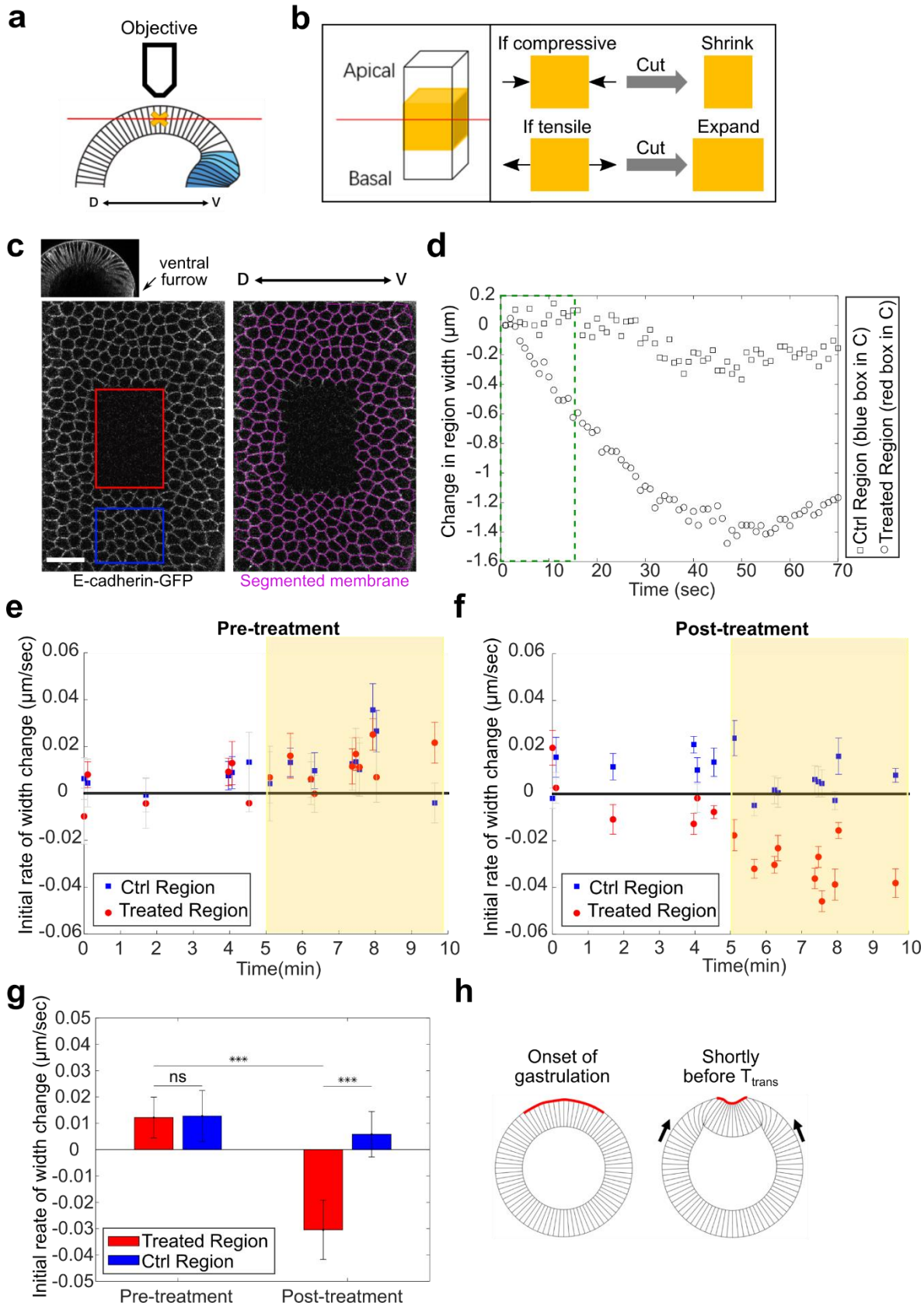

1097

Figure 4. Detection of in-plane compressive stresses in the lateral ectoderm before T_{trans}. (a) Cartoon depicting the experimental setup for laser microdissection to detect compressive stresses. The middle region of the ectodermal cells (yellow cross) was cut by a multiphoton laser. Post-dissection tissue movement was recorded by single-plane (red line) fast imaging. **(b)** Left: A zoomed-in view showing a single cell with the laser-treated region marked with yellow. Right: Predicted outcome of laser cutting when the tissue is tensile or compressive. **(c)** Left: single plane image acquired immediately after laser cutting. Red: laser-treated region. Blue: control region. Right: tracked cell membrane. Scale bar: 20 μm. **(d)** Width change of the control and laser-treated regions (as shown in c) over time in an example embryo. The first 15 seconds of the curves (green box) were used to calculate the initial rate of width change as the readout of tissue response. **(e, f)** Initial rate of width change before (e) and after (f) laser treatment. Error bar is 95% confidence interval of the linear fitting of the initial recoil curve. An immediate shrinkage of the cut region is evident in embryos at the stage 5 – 10 minutes into gastrulation (yellow shaded region). **(g)** Average initial rate of width change in embryos between 5 – 10 minutes into gastrulation. Error bar shows s.d.; N = 10 embryos. ***: $p < 0.001$. Student's t-test. **(h)** Cartoon illustrating the buildup of ectodermal compression after the onset of gastrulation but before T_{trans}.

Figure 5

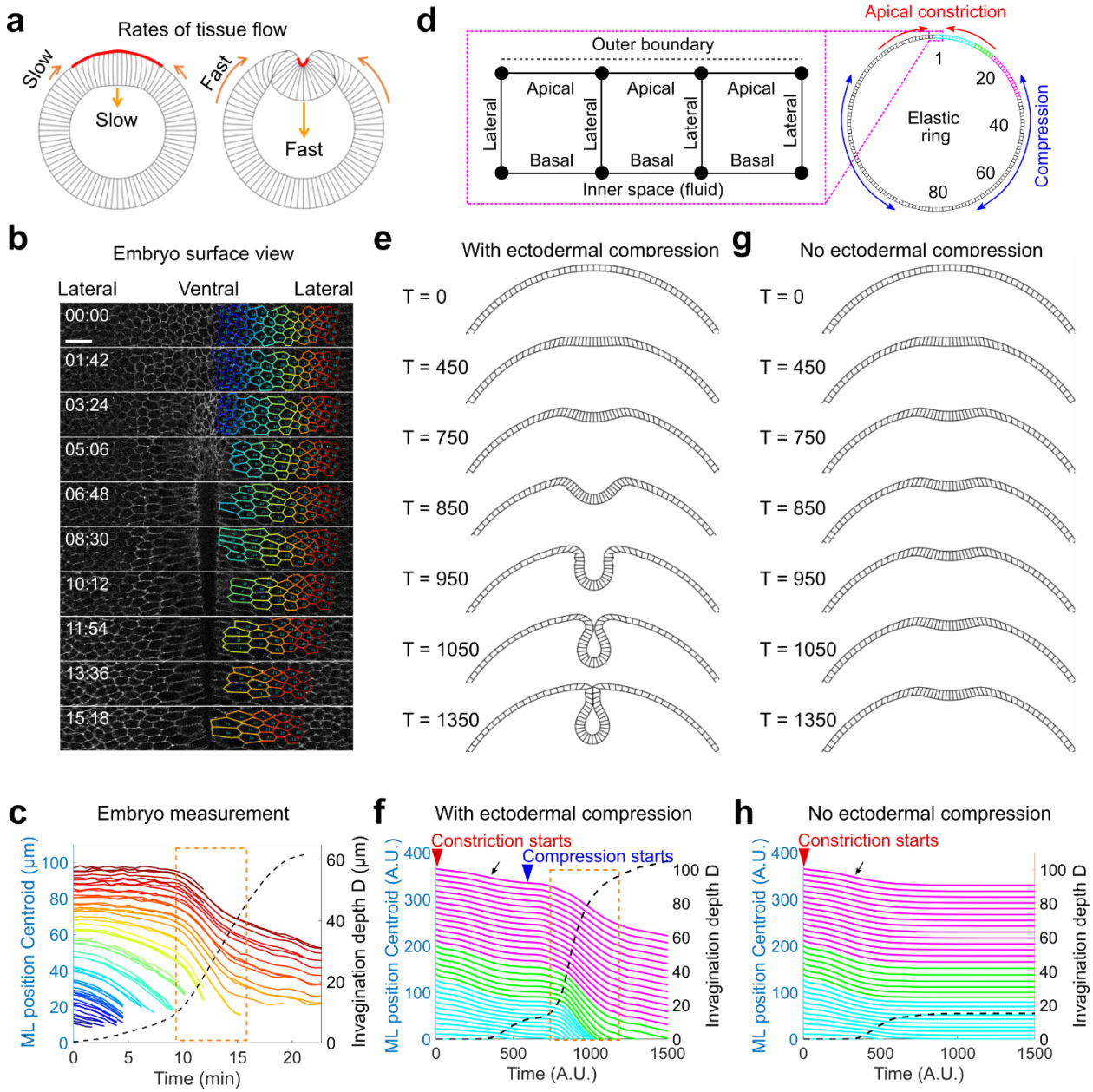

1114

Figure 5. Vertex dynamics model incorporating both apical constriction and in-plane compression recapitulates real tissue dynamics during ventral furrow formation. (a) Cartoon showing the predicted acceleration of tissue deformation (orange arrows) after T_{trans} that resembles the "snap-through" during an elastic buckling process. **(b)** Surface view of an embryo showing tracked cell outlines during ventral furrow formation. Scale bar: 20 μm**. (c)** The relation between cell movement towards ventral midline (solid lines) and the invagination depth D (dotted line) in real embryos. Each solid line represents a single cell, and the color of the lines corresponds to the color of the cell outlines in (b). The rapid acceleration in mesoderm invagination and ectoderm movement happens immediately after T_{trans} (dashed orange box). Shown is a representative measurement out of N = 3 embryos. **(d)** Vertex dynamics model simulating the behavior of a ring-shaped elastic monolayer undergoing localized apical constriction in the presence or absence of in-plane compressive stresses. The numbers indicate the IDs of cells at the right half of the ring. Three groups of cells analyzed for their ventral movement in (f) and (h) are highlighted with colors. **(e)** Simulated morphological change over time with ectodermal compression. **(f)** Relationship between simulated cell movement towards the ventral midline (solid lines) and invagination depth D (dashed line) in the presence of compressive stresses. The solid lines are color coded according to the cell color in (d). Dashed orange box highlights the acceleration of tissue deformation. Black arrow indicates a slight movement of the ectodermal cells during the apical constriction phase which is not observed in real embryos. **(g, h)** The model predicts that in the absence of compression, furrow formation arrests at an intermediate stage resembling T_{trans}. (g) and (h) have a similar layout as (e) and (f), respectively.

Figure 6

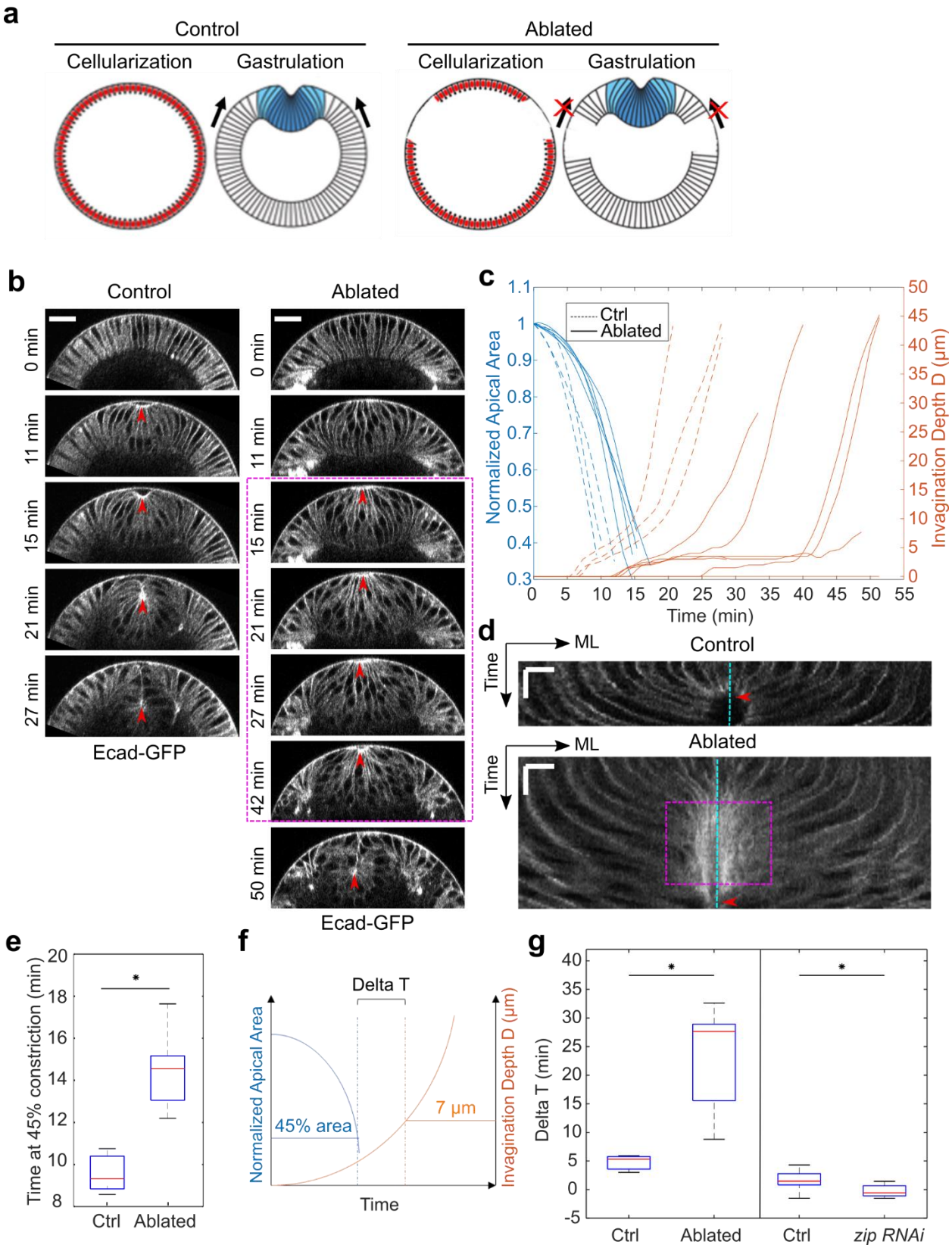

1137

Figure 6. Laser ablation of the lateral ectoderm results in a pause of mesoderm invagination at T_{trans}. (a) A focused multiphoton laser beam is used to ablate cleavage furrows in the lateral ectodermal regions during cellularization, which disrupts cell formation in the ablated regions. As a result, the mesoderm is separated from the rest part of the embryo and become mechanically isolated. **(b)** Cross-section views showing the delayed ventral furrow invagination in ablated embryos. Red arrowheads indicate the apex of the ventral most cells. Magenta box highlights the pause near T_{trans}. Scale bars: 25 μm. **(c)** Invagination depth D and the apical area of the constricting cells in control (N = 3) and ablated (N = 7) embryos during the course of ventral furrow formation. **(d)** Kymographs of apical cell membrane on the ventral surface illustrating the pause near T_{trans} in ablated embryos (magenta box). ML: medial-lateral. Cyan line: ventral midline. Red arrowheads indicate the time when the constricting cells disappear from the surface view. Scale bars: horizontal, 25 μm; vertical: 10 min. **(e)** Time for the constricting cells to achieve 45% constriction after the onset of gastrulation in control and ablated embryos. **(f)** Diagram illustrating how Delay at T_{trans} (Delta T) is defined. Delta T is defined as the time difference between the time when cell reaches 45% constriction and the time when invagination depth D reaches 7 μm. **(g)** Comparison of Delta T between non-ablated and ablated embryos, as well as between the control (N = 9) and *zip RNAi* (N = 8) embryos. *zip RNAi* embryos showed no increase in Delta T despite the reduced rate of apical constriction similar to that in the ablated embryos (Supplementary Figure 10). All statistical comparisons were performed using two-sided Wilcoxon rank sum test. *: $p < 0.05$.

Figure 7

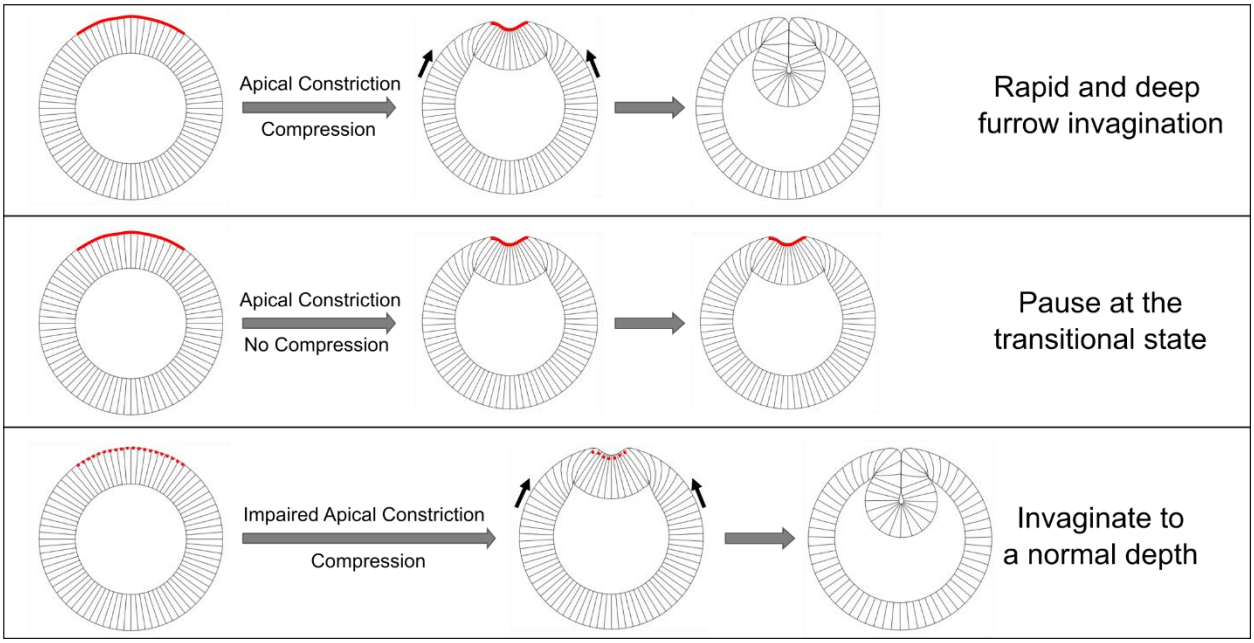

Figure 7. *Drosophila* mesoderm invagination requires a joint action of apical constriction and in-plane compression. Cartoon demonstrating the coordination between apical constriction in the mesoderm and in-plane compression from the ectoderm during ventral furrow formation. The combined action of apical constriction and compression facilitates mesoderm invagination by triggering epithelial buckling. When ectodermal compression is absent (e.g., when the lateral ectoderm is ablated), transition from apical constriction to invagination is greatly delayed, and the embryo pauses at the transition stage for an extended time. When ectodermal compression is intact but apical constriction is partially impaired (e.g., Early Group embryos or *zip RNAi* embryos), the presence of ectodermal compression allows the mesoderm to invaginate to a depth similar to that in the wildtype embryos.